nature astronomy

SUPPLEMENTARY INFORMATION
https://doi.org/10.1038/s41550-018-0430-3

In the format provided by the authors and unedited.

# Extreme magnification of an individual star at redshift 1.5 by a galaxy-cluster lens

**Patrick L. Kelly[1,2*], Jose M. Diego[3], Steven Rodney[4], Nick Kaiser[5], Tom Broadhurst[6,7], Adi Zitrin[8], Tommaso Treu[9], Pablo G. Pérez-González[10], Takahiro Morishita[9,11,12], Mathilde Jauzac[13,14,15], Jonatan Selsing[16], Masamune Oguri[17,18,19], Laurent Pueyo[20], Timothy W. Ross[1], Alexei V. Filippenko[1,21], Nathan Smith[22], Jens Hjorth[16], S. Bradley Cenko[23,24], Xin Wang[9], D. Andrew Howell[25,26], Johan Richard[27], Brenda L. Frye[22], Saurabh W. Jha[28], Ryan J. Foley[29], Colin Norman[30], Marusa Bradac[31], Weikang Zheng[1], Gabriel Brammer[20], Alberto Molino Benito[32], Antonio Cava[33], Lise Christensen[16], Selma E. de Mink[34], Or Graur[35,36], Claudio Grillo[16,37], Ryota Kawamata[38], Jean-Paul Kneib[39], Thomas Matheson[40], Curtis McCully[25,26], Mario Nonino[41], Ismael Pérez-Fournon[42,43], Adam G. Riess[20,30], Piero Rosati[44], Kasper Borello Schmidt[45], Keren Sharon[46] and Benjamin J. Weiner[22]**

[1]Department of Astronomy, University of California, Berkeley, CA, USA. [2]School of Physics and Astronomy, University of Minnesota, Minneapolis, MN, USA. [3]IFCA, Instituto de Física de Cantabria (UC-CSIC), Santander, Spain. [4]Department of Physics and Astronomy, University of South Carolina, Columbia, SC, USA. [5]Institute for Astronomy, University of Hawaii, Honolulu, HI, USA. [6]Department of Theoretical Physics, University of the Basque Country, Bilbao, Spain. [7]IKERBASQUE, Basque Foundation for Science, Alameda Urquijo, Bilbao, Spain. [8]Physics Department, Ben-Gurion University of the Negev, Beer-Sheva, Israel. [9]Department of Physics and Astronomy, University of California, Los Angeles, CA, USA. [10]Departamento de Astrofísica, Facultad de critical curve. Físicas, Universidad Complutense de Madrid, Madrid, Spain. [11]Astronomical Institute, Tohoku University, Sendai, Japan. [12]Institute for International Advanced Research and Education, Tohoku University, Sendai, Japan. [13]Centre for Extragalactic Astronomy, Department of Physics, Durham University, Durham, UK. [14]Institute for Computational Cosmology, Durham University, Durham, UK. [15]Astrophysics and Cosmology Research Unit, School of Mathematical Sciences, University of KwaZulu-Natal, Durban, South Africa. [16]Dark Cosmology Centre, Niels Bohr Institute, University of Copenhagen, Copenhagen, Denmark. [17]Research Center for the Early Universe, University of Tokyo, Tokyo, Japan. [18]Department of Physics, University of Tokyo, Tokyo, Japan. [19]Kavli Institute for the Physics and Mathematics of the Universe (Kavli IPMU, WPI), University of Tokyo, Kashiwa, Japan. [20]Space Telescope Science Institute, Baltimore, MD, USA. [21]Miller Institute for Basic Research in Science, University of California, Berkeley, CA, USA. [22]Steward Observatory, University of Arizona, Tucson, AZ, USA. [23]Astrophysics Science Division, NASA Goddard Space Flight Center, Greenbelt, MD, USA. [24]Joint Space-Science Institute, University of Maryland, College Park, MD, USA. [25]Las Cumbres Observatory, Goleta, CA, USA. [26]Department of Physics, University of California, Santa Barbara, CA, USA. [27]Univ. Lyon, Univ. Lyon1, ENS de Lyon, CNRS, Centre de Recherche Astrophysique de Lyon UMR5574, Saint-Genis-Laval, France. [28]Department of Physics and Astronomy, Rutgers, The State University of New Jersey, Piscataway, NJ, USA. [29]Department of Astronomy and Astrophysics, UCO/Lick Observatory, University of California, Santa Cruz, CA, USA. [30]Department of Physics and Astronomy, The Johns Hopkins University, Baltimore, MD, USA. [31]Department of Physics, University of California, Davis, CA, USA. [32]Instituto de Astronomia, Geofísica e Ciências Atmosféricas, Universidade de São Paulo, São Paulo, Brazil. [33]Department of Astronomy, University of Geneva, Versoix, Switzerland. [34]Anton Pannekoek Institute for Astronomy, University of Amsterdam, Amsterdam, The Netherlands. [35]Harvard-Smithsonian Center for Astrophysics, Cambridge, MA, USA. [36]Department of Astrophysics, American Museum of Natural History, New York, NY, USA. [37]Dipartimento di Fisica, Universitá degli Studi di Milano, Milan, Italy. [38]Department of Astronomy, Graduate School of Science, The University of Tokyo, Tokyo, Japan. [39]Laboratoire d'Astrophysique, Ecole Polytechnique Federale de Lausanne (EPFL), Observatoire de Sauverny, Versoix, Switzerland. [40]National Optical Astronomical Observatory, Tucson, AZ, USA. [41]INAF, Osservatorio Astronomico di Trieste, Trieste, Italy. [42]Instituto de Astrofisica de Canarias (IAC), San Cristóbal de La Laguna, Spain. [43]Universidad de La Laguna, Dpto. Astrofisica, San Cristóbal de La Laguna, Spain. [44]Dipartimento di Fisica e Scienze della Terra, Universitá degli Studi di Ferrara, Ferrara, Italy. [45]Leibniz-Institut fur Astrophysik Potsdam (AIP), Potsdam, Germany. [46]University of Michigan, Department of Astronomy, Ann Arbor, MI, USA.
*e-mail: plkelly@umn.edu

# Supplementary information: Extreme magnification of an individual star at redshift 1.5 by a galaxy-cluster lens

Patrick L. Kelly, Jose M. Diego, Steven Rodney, Nick Kaiser, Tom Broadhurst, Adi Zitrin, Tommaso Treu, Pablo G. Pérez-González, Takahiro Morishita, Mathilde Jauzac, Jonatan Selsing, Masamune Oguri, Laurent Pueyo, Timothy W. Ross, Alexei V. Filippenko, Nathan Smith, Jens Hjorth, S. Bradley Cenko, Xin Wang, D. Andrew Howell, Johan Richard, Brenda L. Frye, Saurabh W. Jha, Ryan J. Foley, Colin Norman, Marusa Bradac, Weikang Zheng, Gabriel Brammer, Alberto Molino Benito, Antonio Cava, Lise Christensen, Selma E. de Mink, Or Graur, Claudio Grillo, Ryota Kawamata, Jean-Paul Kneib, Thomas Matheson, Curtis McCully, Mario Nonino, Ismael Perez-Fournon, Adam G. Riess, Piero Rosati, Kasper Borello Schmidt, Keren Sharon, & Benjamin J. Weiner

**Simulation Using Stars Near Center of 30 Doradus.** We used the SIMBAD (http://simbad.u-strasbg.fr/simbad/) catalog to retrieve information for objects in the H II region 30 Doradus in the LMC. Stars were first selected from the catalog having *V*-band magnitudes and closer than 20′ to its center ($\sim$ 280 pc). We include objects classified as stars, and exclude F,G,K, or M type stars unless they are classified as supergiants. Using a distance of 49 kpc to the LMC, we calculated the stars' absolute magnitudes $M_V$, and their distances from the center of the cluster. For 10,000 trials, we randomly placed the cluster's CC within 20 pc of the 30 Doradus' center, and rotated the stars around the center of 30 Doradus by an angle drawn from a uniform distribution. We find a probability of $\sim 1\%$ of finding a star with a persistent average brightness of at least 27.7 mag, and we find that such a star will also be responsible for $\gtrsim 99\%$ of <26 mag microlensing events. These probabilities are similar to those we estimated from our simulation where the positions of luminous stars near the CC were drawn randomly from a uniform distribution

**Slope of Stellar Luminosity Function in 30 Doradus.** We have also used the SIMBAD catalog of stellar sources to estimate the stellar luminosity function of bright stars in 30 Doradus. Placing stars in 0.5 mag bins by their absolute $V$-band magnitudes, we measure a power-law index of $\alpha \approx -2$. No correction is applied for crowding, or the binary fraction.

**Slope of the Stellar Luminosity Function in Nearby Galaxies.** Stars found in OB associations in seven nearby galaxies observed with *HST* show a luminosity function of $\alpha = 2.53 \pm 0.08$[1]. The stellar luminosity function for stars more luminous than $M_V < -8.5$ mag is not well constrained, the number counts of the $M_V < -8.5$ mag stars in this study are consistent with the slope measured for stars with $-8.5 < M_V < -5$ mag. The slope of $\alpha = 2.53 \pm 0.08$ agrees approximately with a separate earlier analysis[2], which studied the slope of the upper end of the stellar luminosity function of the bluest stars in nearby galaxies using ground-based imaging and found $\alpha = 2.68 \pm 0.08$, although the latter analysis extended only to $M_V \approx -9.5$ mag [see Fig. 7 of Ref. 2]. A second census of the stellar population in galaxy M101 shows that it may host a small number of luminous stars with absolute magnitude $-10 \lesssim M_V \lesssim -11$ [see Fig. 7 of Ref. 3].

The luminosity function of OB associations[4] can be well described by a power-law function having an index $\alpha \approx 2$. The luminosity function of star-forming regions may become flatter in galaxies with higher star-formation rates and star-formation rate densities[5].

**Ground-Based Follow-up Campaigns.** We observed the field with direct imaging with the Low Resolution Imaging Spectrometer (LRIS)[6] on the Keck-I 10 m telescope on 6 May 2016 (PI Filippenko). Director's Discretionary programs with the GTC (PI Pérez González; GTC2016-052), the Very Large Telescope (PI Selsing; 297.A-5026), Gemini North (PI Kelly; GN-2016A-DD-8), and the Discovery Channel Telescope (PI Cenko) obtained follow-up imaging in optical bandpasses.

**Detection from the Ground with the Gran Telescopio Canarias.** We obtained *i*'-band observations of the MACS J1149 field with the 10.4 m Gran Telescopio Canarias (GTC) on 6 June 2016 and 7 June 2016, after the May 2016 peak. To estimate the flux at LS1's position, we extracted the flux inside several apertures with diameters within 1–2 times the the PSF FWHM, and applied aperture corrections to obtain integrated fluxes. The flux estimates for the different apertures agree within 0.10–0.15 mag. The *i*'-band AB magnitudes are 27.73 ± 0.52 on 57544.9381 MJD in conditions with 1.0″ seeing and a total integration of 3000 s, and 28.35 ± 0.43 on 57546.9445 MJD in 0.8″ seeing and a total integration of 5430 s.

**Metallicity of the Local Host-Galaxy Environment of LS1.** The gas-phase oxygen abundance of LS1's host galaxy, including that within the immediate environment of SN Refsdal, has been studied using multiple datasets. LS1 and SN Refsdal have similar offsets from the host nucleus (within $\sim 0.5$ kpc), so the local metallicity near LS1's and SN Refsdal's host-galaxy locations should have similar values. Both the CATS model[7] ($\sim 6.7$ kpc and $\sim 7.3$ kpc, respectively) and the GLAFIC model[8] ($\sim 7.9$ kpc and $\sim 8.2$ kpc) find similar nuclear offsets for LS1 and SN Refsdal.

Analysis of Keck-II OSIRIS integral-field unit (IFU) spectra reported a $3\sigma$ upper limit of $12 + \log(\mathrm{O/H}) < 8.67$ dex in the Pettini & Pagel N2 calibration[9] for an H II region $\sim 200$ pc away from SN Refsdal's site. From the same observations, the authors find a combined upper limit of $12 + \log(\mathrm{O/H}) < 8.11$ dex from observations of nine H II regions at nuclear offsets between $\sim 5$ and $\sim 7$ kpc[10], which is similar to the offsets of LS1 and SN Refsdal.

Recent work[11] has analyzed WFC3 grism spectra taken by GLASS[12,13] and follow-up observations of SN Refsdal. They fit the abundance measurement using a linear model,

$$12 + \log(\mathrm{O/H}) = (-0.0666 \pm 0.0232) \times r + 8.82 \pm 0.039 \text{ dex}, \tag{1}$$

where $r$ is the offset from the nucleus in kpc. This yields an abundance at LS1's offset (assuming $7.9 \pm 0.5$ kpc) of $12 + \log(\mathrm{O/H}) = 8.29 \pm 0.19$ dex. This analysis does not take into account the [N II] line when estimating the oxygen abundance, as it can be a biased tracer at $z > 1$[14].

Finally, while [N II] was not detected in the OSIRIS IFU spectra of the site of SN Refsdal[10], a 1 hr Keck-II MOSFIRE integration yielded a [N II] detection. The [N II] line strength yields a

PP04 N2 oxygen abundance of 12 + log(O/H) = 8.3 ± 0.1 dex [15], which is in agreement with the above estimate made using the Maiolino calibration [16] from WFC3 grism spectra.

Given the above grism as well as MOSFIRE [N II] metallicity estimates, we use an oxygen abundance of 12 + log(O/H) ≈ 8.3 dex as the metallicity of the massive stellar population near LS1's coordinates. The Castelli & Kurucz 2004 stellar atmosphere models [17] are parameterised based on the Grevesse & Sauval 1998 [18] solar oxygen abundance of 12 + log(O/H) = 8.83±0.06 dex. Therefore, we adopt $\log(Z/Z_\odot) = -0.5$ when drawing comparisons with the Castelli & Kurucz ATLAS9 models.

**K-correction and Distance Modulus.** We calculate *K*-corrections following Equation 2 of Ref. 19,

$$K = 2.5 \times \log_{10}(1 + z) + m^{\rm AB}_{F125W,\rm syn} - m^{\rm Vega}_{V,\rm syn}, \tag{2}$$

where $z = 1.49$, $m^{\rm AB}_{F125W,\rm syn}$ is the WFC3 $F125W$ synthetic magnitude of a redshifted model spectrum, and $m^{\rm Vega}_{V,\rm syn}$ is the synthetic Johnson *V*-band magnitude of the rest-frame model spectrum. Here the *K*-correction $K_{\rm xy}$ is defined as

$$m_{\rm y} = M_{\rm x} + dm + K_{\rm xy}, \tag{3}$$

where $m_{\rm y}$ is the observer-frame apparent magnitude in the y band, $M_{\rm x}$ is the rest-frame absolute magnitude in the x band, and $dm$ is the distance modulus. Using the best-fitting spectral models, we calculate $K_{V,F125W} = -1.10$ mag, and adopt $dm = 45.21$ mag at $z = 1.49$ (with no correction for magnification).

**Stellar-Mass Density Along the Line of Sight to LS1.** We computed two separate estimates of the stellar-mass density to LS1. The first estimate was the value we used when we created most of the simulated light curves, but it excluded light from the nearby brightest cluster galaxy (BCG). We computed a second, improved estimate that accounted for all intracluster light (ICL) along the line of sight. The updated analysis yielded a density approximately twice as high as the initial value.

**Initial Estimate:** Galaxies with $m_{\mathrm{F160W}} < 26$ AB mag are selected and fit with single Sérsic profiles by using GALFIT[20] in a postage stamp (300 pix × 300 pix). At the same time, the local sky background, assumed to be constant across the stamp, is fitted with the galaxy light profile. After fitting all the galaxies in the field, we reconstruct the ICL map by using the estimated local sky background values. Overlapping pixels are stacked, weighted by the $\chi^2_\nu$ value from the fit. The uncertainty is estimated from the original root-mean-square (RMS) map (published by the *Hubble* Frontier Fields team) and the systematic differences caused by changing the stamp size. We repeat this procedure for the ACS WFC $F435W$, $F606W$, $F814W$, and WFC3 IR $F105W$, $F125W$, $F140W$, and $F160W$ filter bands[21]. A correction is applied for Galactic extinction[22].

Stellar mass is estimated in each pixel using the Fitting and Assessment of Synthetic Templates (FAST) software tool[23] with the BC03[24] stellar population model. FAST uses the Galaxy Spectral Evolution Library (GALAXEV; http://www.bruzual.org/) code to assemble composite stellar populations. We use the BC03 isochrones, a Chabrier IMF, and an exponentially declining star-formation history. Stars have initial masses that are between 0.1 and 100 $M_\odot$, and models are computed for metallicities of 0.004, 0.008, 0.02, and 0.05. The hot gas in the galaxy-cluster ICM is thought to destroy dust, and extinction from dust is assumed to be zero. We note, however, that allowing the dust extinction to be a free parameter would change the estimated stellar mass by $< 1\%$.

**Revised Estimate:** We calculated a second estimate for the stellar-mass density that includes the contribution of stellar light associated with the BCG. We first constructed a total of eight apertures around the BCG shown in Supplementary Figure 8. The apertures' offsets from the BCG center and $F140W$ surface brightnesses are similar to those of LS1, and were selected to exclude point sources and cluster-member galaxies (except the BCG).

We estimate ACS WFC $F435W$, $F606W$, $F814W$, and WFC3 IR $F105W$, $F125W$, $F140W$, and $F160W$ fluxes within each aperture, and apply a correction for Galactic extinction[22]. We next determine the ratio between the stellar mass ($M_*$) and the WFC3-IR $F140W$ flux ($L$) within each aperture. We estimate $M_*$ with FAST[23] and the BC03[24] stellar population synthesis models. We adopt a delayed exponentially declining star-formation history and include both subsolar and solar metallicity ($\sim$ 0.02 and 0.008) populations. Separate model fits are made for Chabrier and Salpeter IMFs, and the stars in our BC03 population synthesis models have initial masses that are between 0.1 and 100 $M_\odot$.

Within each aperture, the statistical uncertainties of the total WFC3-IR flux in each bandpass are $\lesssim 0.5\%$. Among fits within the apertures, the average $e$-folding time is $\sim$ 600 Myr, and, at redshift $z = 0.54$, the stellar population ages are, on average, $\sim$ 4 Gyr. The uncertainty in $M_\star/L$ for each aperture is $\sim 30\%$, which approximately equals the standard deviation among the best-fitting estimates for all apertures.

To estimate the stellar-mass density along the line of sight to LS1, we multiply the mean $M_*/L$ computed across all eight apertures by the average $F140W$ surface brightness in the two apertures adjacent to LS1. These apertures adjacent to LS1 may contain contamination in observer-frame optical bandpasses from the underlying, young lensed galaxy. Within the WFC3-IR $F140W$ bandpass, however, light from the cluster dominates.

For Chabrier and Salpeter IMFs, the stellar mass densities computed using the BC03 model are $1.1^{+0.3}_{-0.3} \times 10^7\,\mathrm{M_\odot\,kpc^{-2}}$ and $1.9^{+0.6}_{-0.6} \times 10^7\,\mathrm{M_\odot\,kpc^{-2}}$, respectively. These revised estimates as well as our initial estimate for the density include remnants, whose masses are computed using the Renzini "initial–final" mass function[25]. The total local projected mass density inferred from cluster models[7,26,27] is $\sim 2 \times 10^9\,\mathrm{M_\odot\,kpc^{-2}}$.

**Data Availability:** The data that support the plots within this paper and other findings of this study are available from the corresponding author upon reasonable request.


1. Bresolin, F. *et al.* A Hubble Space Telescope Study of Extragalactic OB Associations. *Astron. J.* **116**, 119–130 (1998).

2. Freedman, W. L. The upper end of the stellar luminosity function for a sample of nearby resolved late-type galaxies. *Astrophys. J.* **299**, 74–84 (1985).

3. Grammer, S. & Humphreys, R. M. The Massive Star Population in M101. I. The Identification and Spatial Distribution of the Visually Luminous Stars. *Astron. J.* **146**, 114 (2013).

4. Bastian, N. *et al.* Hierarchical star formation in M33: fundamental properties of the star-forming regions. *Mon. Not. R. Astron. Soc.* **379**, 1302–1312 (2007).

5. Cook, D. O. *et al.* The connection between galaxy environment and the luminosity function slopes of star-forming regions. *Mon. Not. R. Astron. Soc.* **462**, 3766–3799 (2016).

6. Oke, J. B. *et al.* The Keck Low-Resolution Imaging Spectrometer. *Publ. Astron. Soc. Pac.* **107**, 375 (1995).

7. Jauzac, M. *et al.* Hubble Frontier Fields: predictions for the return of SN Refsdal with the MUSE and GMOS spectrographs. *Mon. Not. R. Astron. Soc.* **457**, 2029–2042 (2016).

8. Kawamata, R., Oguri, M., Ishigaki, M., Shimasaku, K. & Ouchi, M. Precise Strong Lensing Mass Modeling of Four Hubble Frontier Field Clusters and a Sample of Magnified High-redshift Galaxies. *Astrophys. J.* **819**, 114 (2016).

9. Pettini, M. & Pagel, B. E. J. [OIII]/[NII] as an abundance indicator at high redshift. *Mon. Not. R. Astron. Soc.* **348**, L59–L63 (2004).

10. Yuan, T., Kobayashi, C. & Kewley, L. J. H II Region Metallicity Constraints Near the Site of the Strongly Lensed Supernova SN Refsdal at Redshift 1.49. *Astrophys. J. Lett.* **804**, L14 (2015).

11. Wang, X. *et al.* The Grism Lens-amplified Survey from Space (GLASS). X. Sub-kiloparsec Resolution Gas-phase Metallicity Maps at Cosmic Noon behind the Hubble Frontier Fields Cluster MACS1149.6+2223. *Astrophys. J.* **837**, 89 (2017).

12. Schmidt, K. B. *et al.* Through the Looking GLASS: HST Spectroscopy of Faint Galaxies Lensed by the Frontier Fields Cluster MACSJ0717.5+3745. *Astrophys. J. Lett.* **782**, L36 (2014).

13. Treu, T. *et al.* The Grism Lens-Amplified Survey from Space (GLASS). I. Survey overview and first data release. *Astrophys. J.* **812**, 114 (2015).

14. Steidel, C. C. *et al.* Strong Nebular Line Ratios in the Spectra of z ˜ 2-3 Star Forming Galaxies: First Results from KBSS-MOSFIRE. *Astrophys. J.* **795**, 165 (2014).

15. Kelly, P. L. *et al.* SN Refsdal: Classification as a Luminous and Blue SN 1987A-like Type II Supernova. *Astrophys. J.* **831**, 205 (2016).

16. Maiolino, R. *et al.* AMAZE. I. The evolution of the mass-metallicity relation at z ¿ 3. *Astron. Astrophys.* **488**, 463–479 (2008).

17. Castelli, F. & Kurucz, R. L. New Grids of ATLAS9 Model Atmospheres. Preprint at `https://arxiv.org/abs/astro-ph/0405087` (2004).

18. Grevesse, N. & Sauval, A. J. Standard Solar Composition. *Space Sci. Rev.* **85**, 161–174 (1998).

19. Kim, A., Goobar, A. & Perlmutter, S. A Generalized K Correction for Type IA Supernovae: Comparing R-band Photometry beyond z=0.2 with B, V, and R-band Nearby Photometry. *Publ. Astron. Soc. Pac.* **108**, 190 (1996).

20. Peng, C. Y., Ho, L. C., Impey, C. D. & Rix, H.-W. Detailed Structural Decomposition of Galaxy Images. *Astron. J.* **124**, 266–293 (2002).

21. Morishita, T. *et al.* Characterizing Intracluster Light in the Hubble Frontier Fields. *Astrophys. J.* **846**, 139 (2017).

22. Schlegel, D. J., Finkbeiner, D. P. & Davis, M. Maps of Dust Infrared Emission for Use in Estimation of Reddening and Cosmic Microwave Background Radiation Foregrounds. *Astrophys. J.* **500**, 525 (1998).

23. Kriek, M. *et al.* An Ultra-Deep Near-Infrared Spectrum of a Compact Quiescent Galaxy at z = 2.2. *Astrophys. J.* **700**, 221–231 (2009).

24. Bruzual, G. & Charlot, S. Stellar population synthesis at the resolution of 2003. *Mon. Not. R. Astron. Soc.* **344**, 1000–1028 (2003).

25. Renzini, A. & Ciotti, L. Transverse Dissections of the Fundamental Planes of Elliptical Galaxies and Clusters of Galaxies. *Astrophys. J. Lett.* **416**, L49 (1993).

26. Diego, J. M. *et al.* A free-form prediction for the reappearance of supernova Refsdal in the Hubble Frontier Fields cluster MACSJ1149.5+2223. *Mon. Not. R. Astron. Soc.* **456**, 356–365 (2016).

27. Zitrin, A. *et al.* Hubble Space Telescope Combined Strong and Weak Lensing Analysis of the CLASH Sample: Mass and Magnification Models and Systematic Uncertainties. *Astrophys. J.* **801**, 44 (2015).

28. Marigo, P. & Girardi, L. Evolution of asymptotic giant branch stars. I. Updated synthetic TP-AGB models and their basic calibration. *Astron. Astrophys.* **469**, 239–263 (2007).

29. Marigo, P. *et al.* Evolution of asymptotic giant branch stars. II. Optical to far-infrared isochrones with improved TP-AGB models. *Astron. Astrophys.* **482**, 883–905 (2008).

30. Cardelli, J. A., Clayton, G. C. & Mathis, J. S. The relationship between infrared, optical, and ultraviolet extinction. *Astrophys. J.* **345**, 245–256 (1989).

31. Duchêne, G. & Kraus, A. Stellar Multiplicity. *Ann. Rev. Astron. Astr.* **51**, 269–310 (2013).

32. Woosley, S. E., Heger, A. & Weaver, T. A. The evolution and explosion of massive stars. *Rev. Mod. Phys.* **74**, 1015–1071 (2002).

33. Fryer, C. L. *et al.* Compact Remnant Mass Function: Dependence on the Explosion Mechanism and Metallicity. *Astrophys. J.* **749**, 91 (2012).

34. Spera, M., Mapelli, M. & Bressan, A. The mass spectrum of compact remnants from the PARSEC stellar evolution tracks. *Mon. Not. R. Astron. Soc.* **451**, 4086–4103 (2015).

35. Paczynski, B. Gravitational microlensing at large optical depth. *Astrophys. J.* **301**, 503–516 (1986).

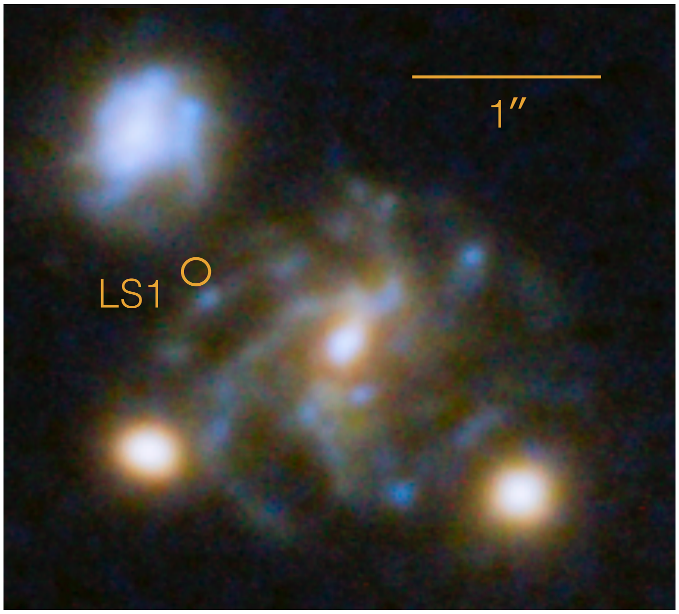


Supplementary Figure 1: **Predicted position of LS1 in separate, full image of its host galaxy created by MACS J1149 galaxy-cluster lens.** LS1's predicted coordinates are marked by the orange circle. The cluster lens create three images of the host galaxy at redshift $z = 1.49$. We detected LS1 adjacent to the critical curve separating two partial, merging images which have opposite parity. The third, full image shown here is at a greater distance from the cluster center, and it shows that LS1 lies close to the tip of a spiral arm.

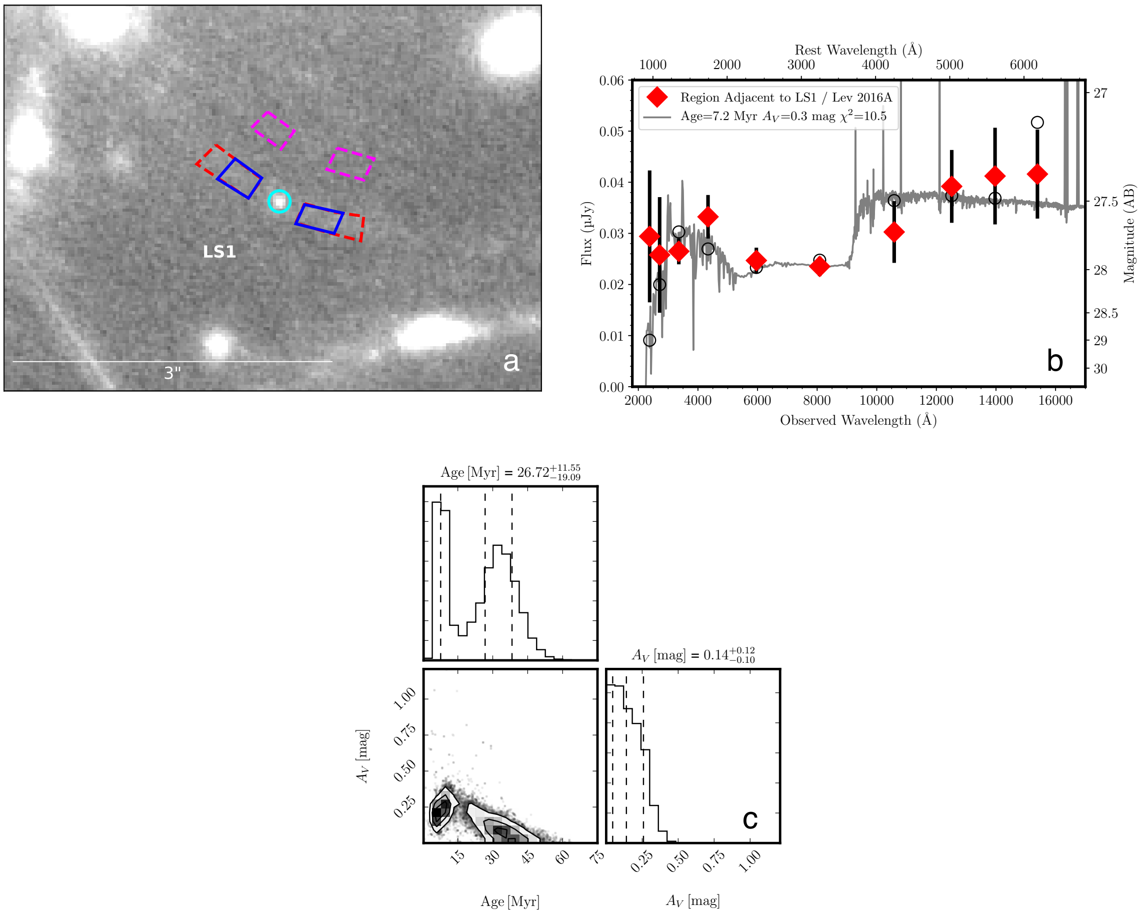

Supplementary Figure 2: **Constraints on the age and dust extinction of the stellar population along the lensed arc adjacent to LS1. a,** LS1's flux was measured in the circular cyan aperture and the background measured inside of the red dashed aperture. **b,** The SED of the underlying arc measured inside the aperture outlined by a blue boundary, after subtracting the background measured in the aperture outlined in magenta. Red diamonds show measured flux densities, and empty black circles correspond to expected flux densities for the best-fitting model. **c,** The posterior probability distributions of the age and extinction $A_V$ of the stellar population. Spectra of the host galaxy favor a gas-phase metallicity of $Z \approx -0.3$. At such a metallicity, we find a bimodel posterior probability distribution with peaks at $\sim 8$ and $\sim 35$ Myr. An age of $\sim 8$ Myr would be consistent with the age of a blue supergiant star. The stellar population synthesis model is constructed using the Padova isochrones[28,29], and we apply a Cardelli extinction law with $R_V = 3.1$[30]. Dashed vertical lines correspond to 16%, 50%, and 84% percentiles of the respective posterior distributions inferred for the age and extinction $A_V$ of the underlying stellar population.

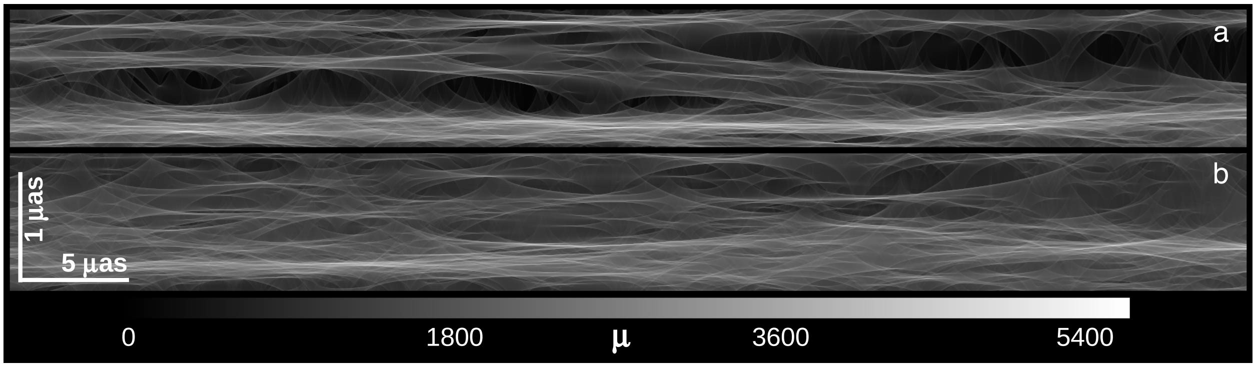


Supplementary Figure 3: **Distinct magnification patterns for respective counterimages Lev16B and LS1/Lev16A of LS1 within the source-plane host galaxy at redshift $z = 1.49$ from a ray-tracing simulation. a,** Extensive regions of low magnification ($\lesssim 100$) for negative-parity image Lev16A could explain why it is undetected in *HST* imaging acquired in all except a single epoch acquired from 2004 through 2017. **b,** The map for positive-parity image LS1/Lev16A lacks such regions of extensive low magnification, and it always detected in deep imaging. Plotted angular scale is in the source plane, and one μarcsec in each panel corresponds to a physical $8.6 \times 10^{-3}$ pc at redshift $z = 1.49$. If LS1 has an apparent transverse velocity of $1000\,\mathrm{km\,s^{-1}}$, it would travel 1 μarcsecond in 8.6 observer-frame years. These ray-tracing simulations are realistic if Lev16B and LS1/Lev16A are mutual counterimages offset by $0.13''$ on opposite sides of the galaxy cluster's critical curve in the image plane, and each of the counterimages has an average magnification of 600. The galaxy-cluster caustic, which is offset by 2.1 pc from these maps, is oriented parallel to the horizontal axes of each panel. The different patterns of magnification correspond to the parity of the image; Lev16B has negative parity, while LS1/Lev16A has positive parity. Here we have created a random realization of foreground intracluster stars and remnants having a mass-density ($1.9^{+0.6}_{-0.6} \times 10^7\,\mathrm{M_\odot\,kpc^{-2}}$) matching that we infer for a Salpeter IMF.

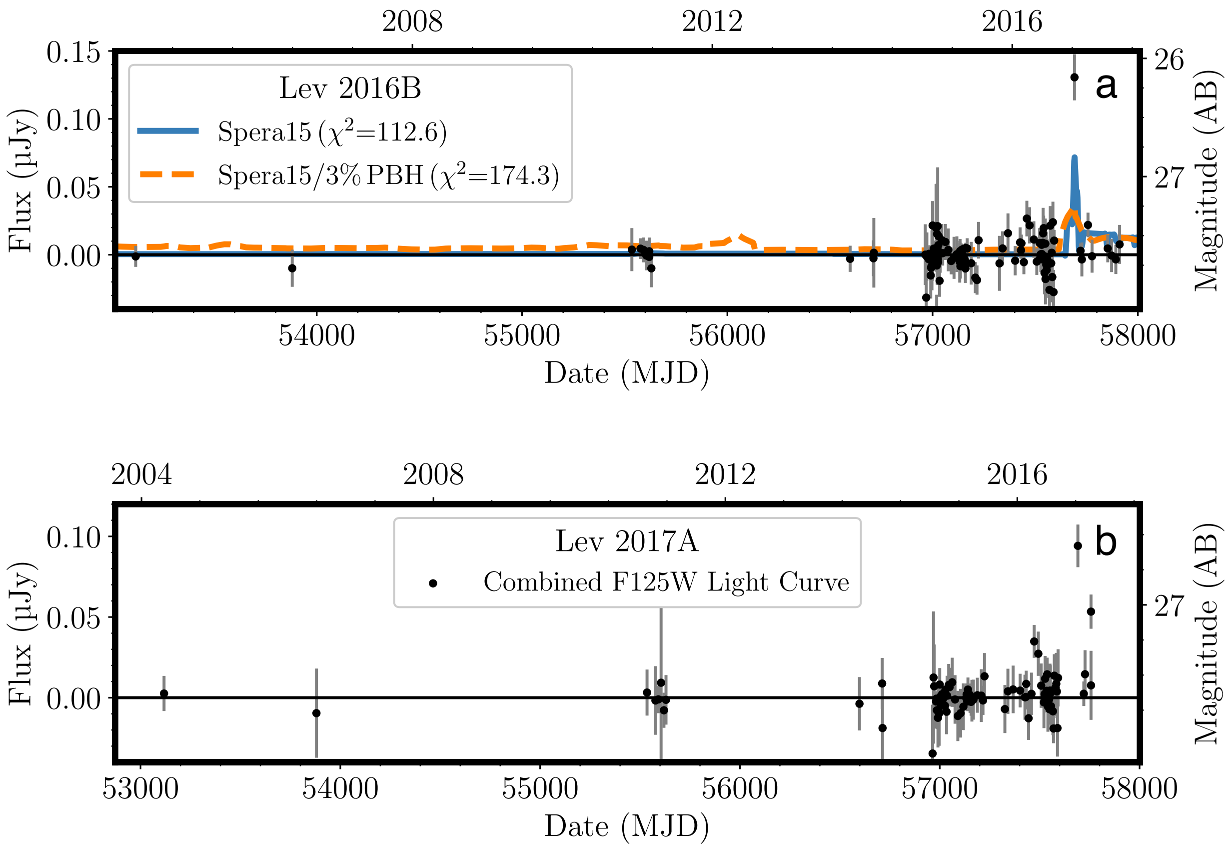


Supplementary Figure 4: **Photometry from *HST* imaging taken from 2004 through 2017 at the locations of Lev16B and Lev 2017A.** Solid blue and dashed orange lines, black circles, and error bars are the same as in Figure 4. **a,** Light curve measured at the position of Lev16B detected on 30 October 2016. **b,** Light curve extracted at the coordinates of potential event Lev 2017A detected on 3 January 2017. Fluxes measured through all wide-band *HST* filters are converted to $F125W$ using LS1's SED. Lev 2017A is only offset from Lev16B by 0.10″, so flux measurements at their positions are correlated. The first (higher) peak in Lev 2017A's light curve plotted here corresponds to flux from Lev16B.

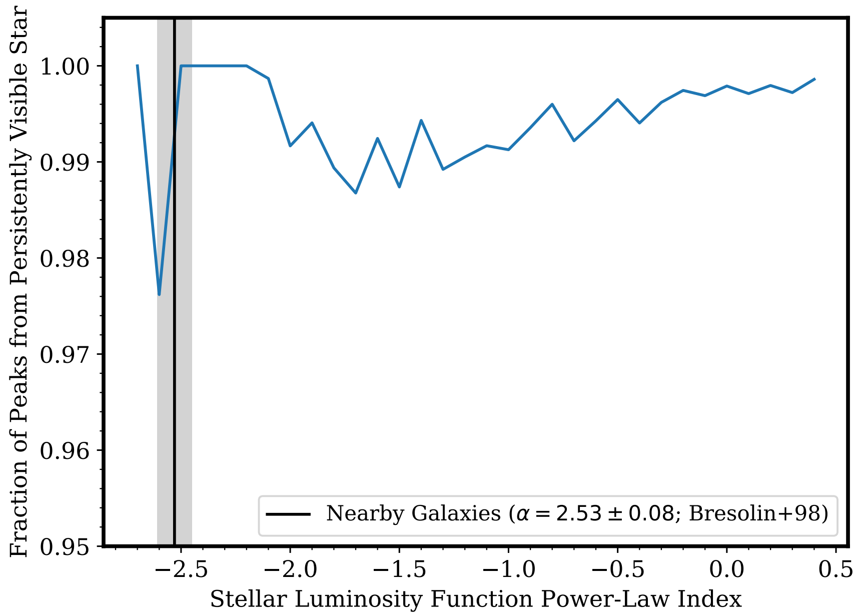


Supplementary Figure 5: **When a lensed star has a bright average apparent magnitude ($F125W$ < 27.7 mag), it will also be responsible for almost all bright microlensing peaks ($F125W$ < 26 mag) observed near the critical curve for simple assumptions.** Here we plot the fraction of bright peaks caused by the bright star against the index of the stellar luminosity function. The solid vertical line and underlying shaded region show the most probable value of and 68% uncertainty on the power-law index of the stellar luminosity function measured in nearby galaxies ($\alpha = -2.53 \pm 0.08$)[1]. Since $\gtrsim$ 99% of events likely arise from the luminous star, it is likely that Lev16B corresponds to the same star as LS1. However, this simulation randomly assigns positions to massive stars. To determine whether the observed clustering of massive stars could yield a greater probability that LS 1 / Lev16A and Lev16B are different stars, we carry out a simulation instead using the observed absolute magnitudes and positions of stars in the 30 Doradus cluster in the LMC from the SIMBAD catalog, and find a similarly low probability.

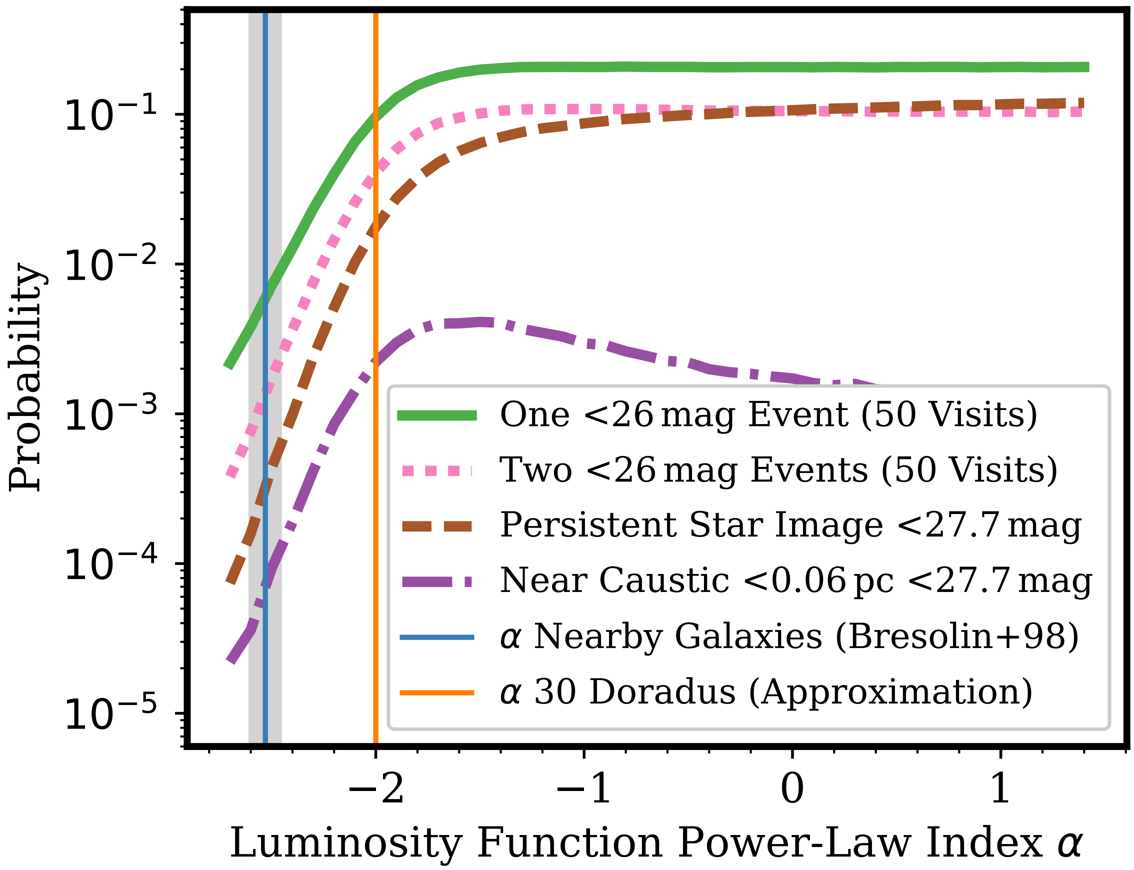


Supplementary Figure 6: **Dependence of the probability of observing highly magnified stellar images on the stellar luminosity function of the underlying arc.** Panel shows probabilities of (a) bright microlensing events ($F125W < 26$ mag; solid green and dotted pink), (b) a persistently bright magnified star ($F125W < 27.7$ mag) similar to that observed at LS1's position in 2004–2017 (dashed brown), and (c) a persistently bright magnified star ($F125W < 27.7$ mag) within 0.06 pc (dot-dash purple). The solid blue vertical line and underlying shaded region show the most probable value of and 68% uncertainty on the power-law index of the stellar luminosity function in nearby galaxies ($\alpha = -2.53 \pm 0.08$)[1]. Probabilities are small given the index of stellar luminosity function measured for nearby galaxies, but become significantly larger for shallower power-law indices, such as that for the 30 Doradus star-forming region in the LMC (vertical orange; approximate). Here we have assumed $N_{\rm obs} = 50$ visits by *HST*, the number of separate observations of MACS J1149 taken through 13 April 2017 after binning data by 10 days. The lower stellar luminosity limit used for these simulations is $10\,L_\odot$.

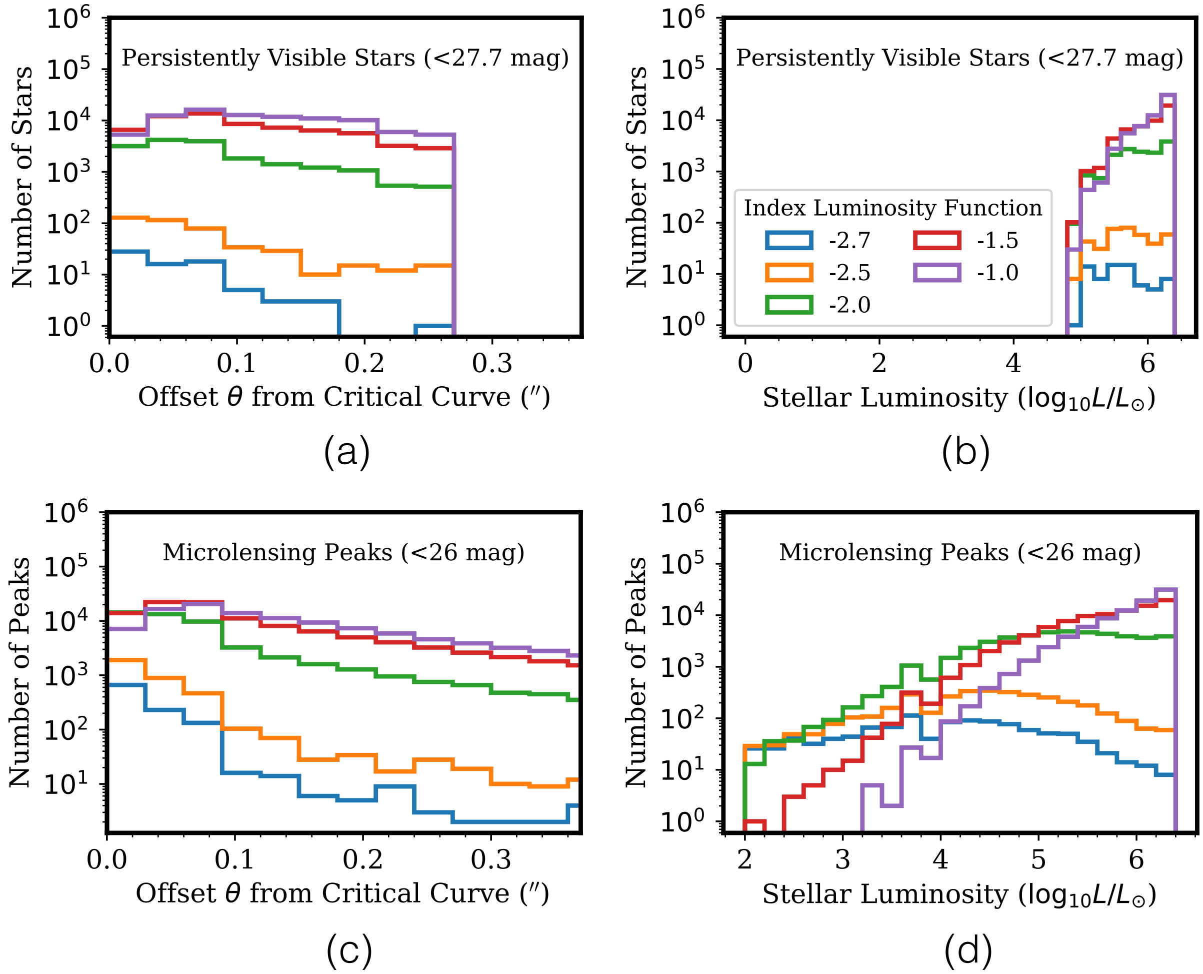


Supplementary Figure 7: **Offsets from critical curve and luminosities of lensed stars for different luminosity functions from $10^6$ Monte Carlo simulations.** We use the surface brightness ($F125W \approx 25\,\mathrm{mag\,arcsec^{-2}}$) measured along the 0.2″-wide arc to constrain the normalization of the stellar luminosity function, and then Poisson statistics to populate the source plane. The lower luminosity limit used for these simulations is $10\,\mathrm{L}_\odot$. **a,b,** Stars with $F125W\ \leq 27.7$ magover a period lasting many years should only appear within $\sim 0.15''$ of the critical curve, and have luminosities of $\gtrsim 10^{5.4}\,\mathrm{L}_\odot$. **c,d,** Expected offset distribution of bright microlensing peaks ($F125W \leq 26$ mag) to 0.4″, and of the luminosities of lensed stars. A stellar luminosity function similar to that measured in nearby galaxies ($\alpha = -2.53 \pm 0.08$) yields fewer events with less-luminous stars[1].

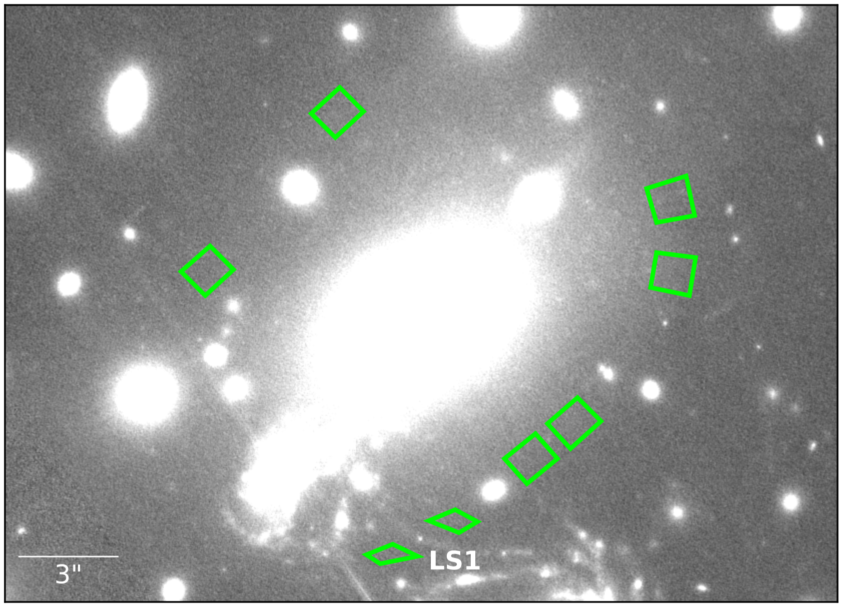


Supplementary Figure 8: **Apertures used for revised estimate of galaxy-cluster stellar-mass density along line-of-sight to LS1.** We first estimate the mean $M_*/L$ across all eight apertures using stellar-population synthesis models. We next multiply the average $F140W$ surface brightness in the two apertures adjacent to LS1 by the mean value of $M_*/L$ to estimate the stellar mass density along the line of sight to LS1.

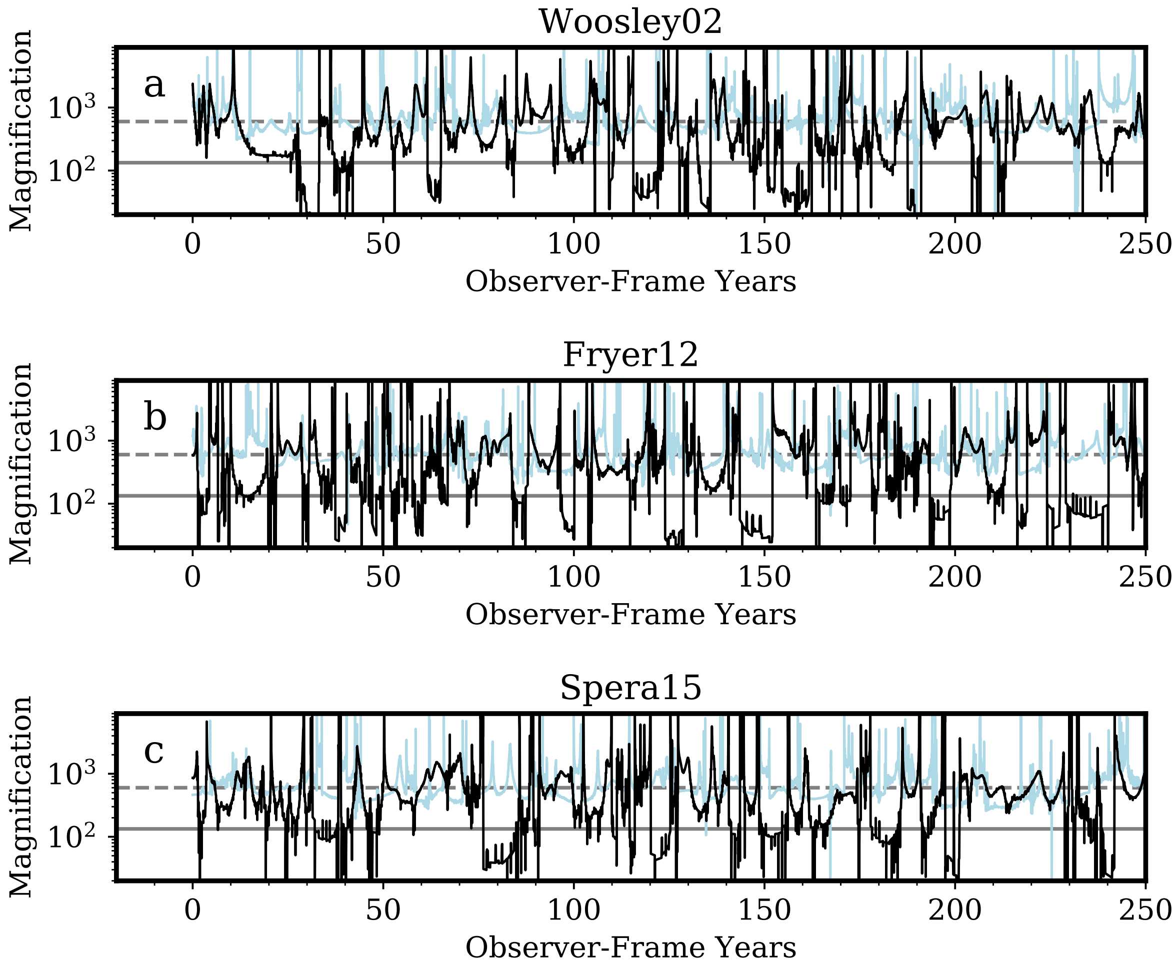


Supplementary Figure 9: **Simulated light curves of a star at $\theta = 0.13''$ from cluster critical curve for three stellar evolution and core-collapse models.** The mass functions are constructed using a Chabrier IMF and a prescription for binary fractions and mass ratios at low redshift[31]. The light blue line shows the simulated light curve for the stellar image at LS1's position, and black line plots the light curve for its counterimage at Lev 16B's position. The stellar evolution models used to determine the initial–final mass function for each star include: **a,** the solar-metallicity, single stellar evolution models (Woosley02)[32]; **b,** single stars at subsolar metallicity ($Z = 0.3\,Z_\odot$; $Z = 0.006$) where BHs with masses up to $30\,M_\odot$ form from the collapse of massive stars (Fryer12)[33]; and **c,** stars having initial masses greater than $\sim 33\,M_\odot$ become BHs with masses within the range $20–50\,M_\odot$ (Spera15)[34]. The Fryer12 and Spera15 models contain greater numbers of BH remnants, which may yield a higher frequency of decade-long intervals with low magnification.

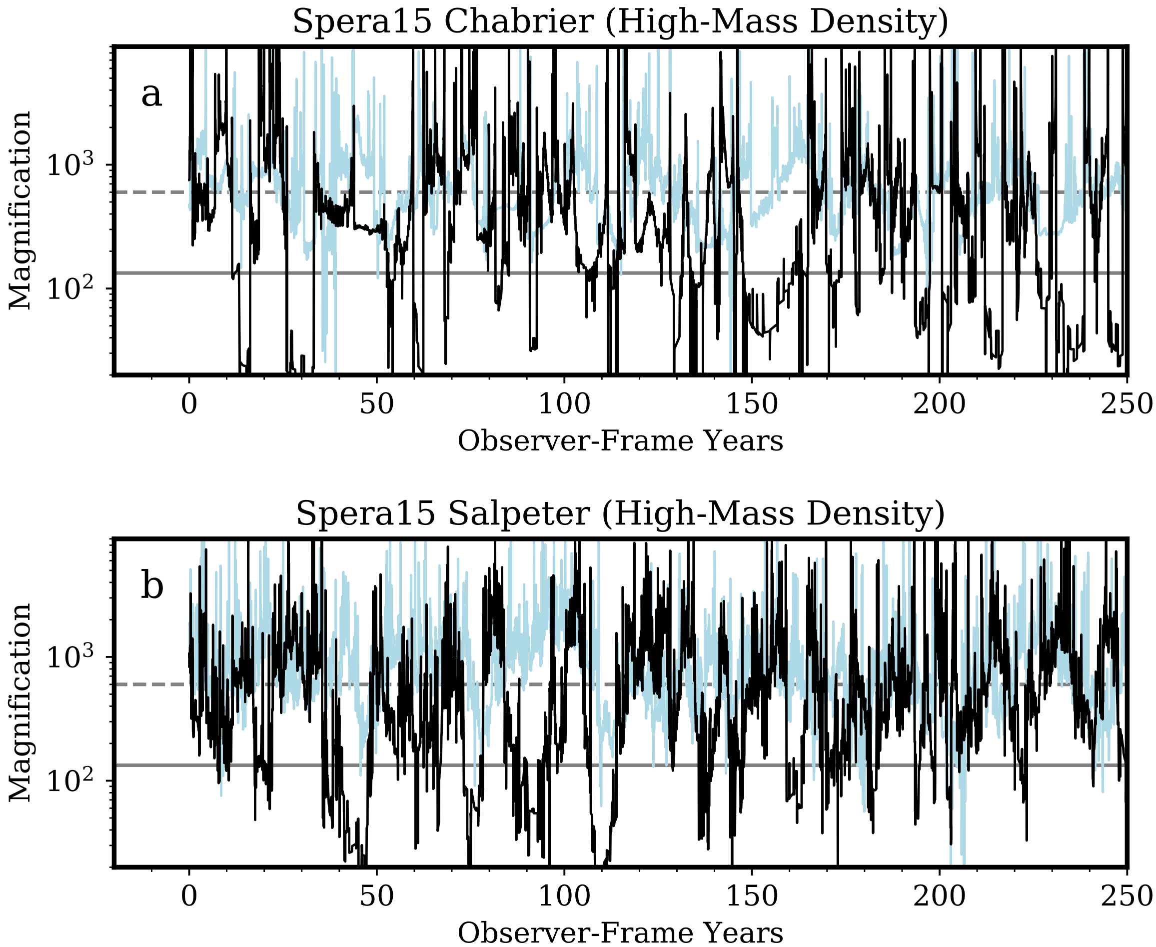


Supplementary Figure 10: **Simulated light curves of a star at $\theta = 0.13''$ from cluster critical curve for Chabrier and Salpeter IMFs.** The light blue line shows the simulated light curve for the stellar image at LS1's position, and black line plots the light curve for its counterimage at Lev 16B's position. **a,** Simulated light curve constructed from the model with a Chabrier IMF. **b,** Light curve simulated from a model instead with a Salpeter IMF. The light curve constructed for a Salpeter IMF contains a greater number of peaks than that constructed for a Chabrier IMF. Plotted models are constructed using a prescription for binary fractions and mass ratios at low redshift[31]. The stellar-mass densities are $1.1^{+0.3}_{-0.3} \times 10^7\ M_\odot\ \mathrm{kpc}^{-2}$ and $1.9^{+0.6}_{-0.6} \times 10^7\ M_\odot\ \mathrm{kpc}^{-2}$ for the Chabrier and Salpeter plots, respectively, and are the best-fitting values to the SED of the ICL for stellar-population synthesis models constructed using Chabrier and Salpeter IMFs.

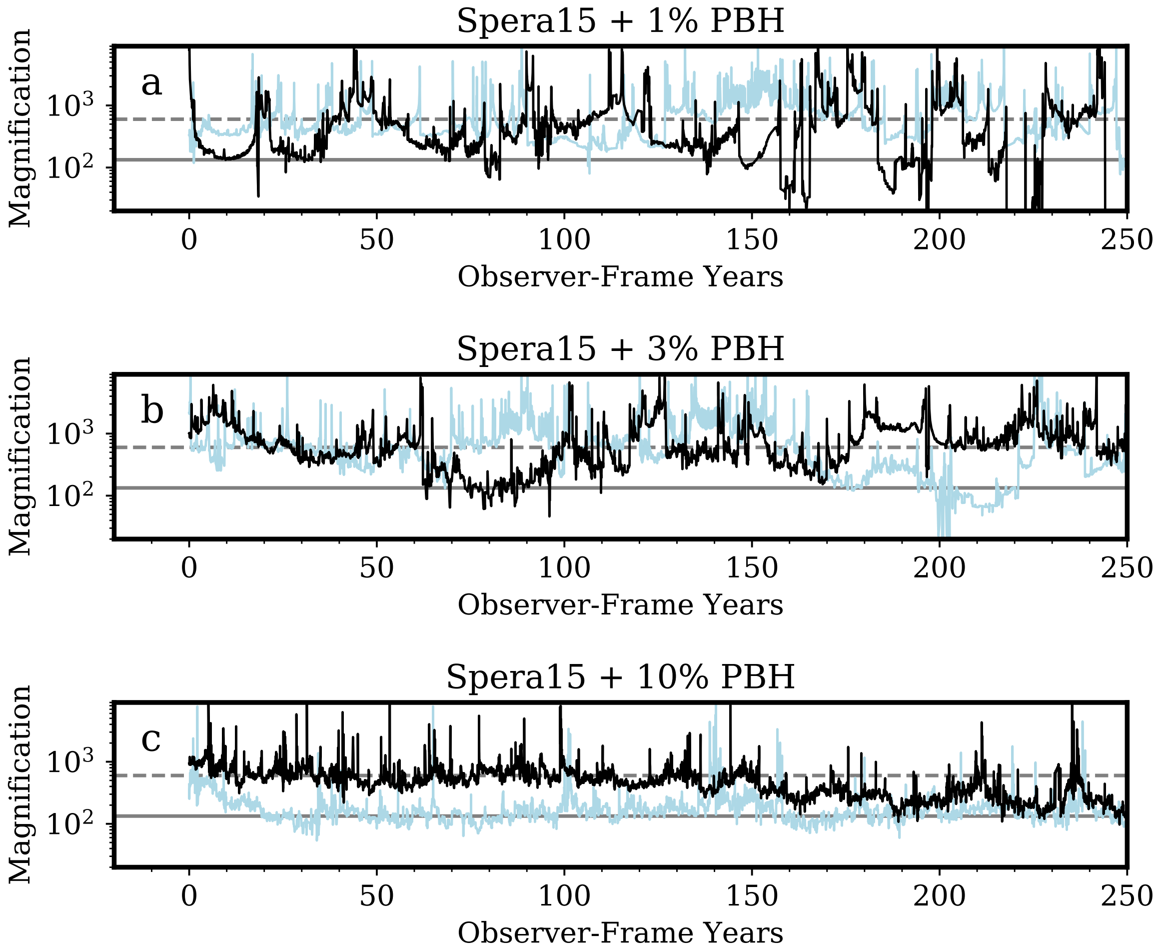


Supplementary Figure 11: **Effect of increasing abundance of 30 $M_\odot$ BHs on the simulated light curves of star at $\theta$ = 0.13″.** The light blue line shows the simulated light curve for the stellar image at LS1's position, and black line plots the light curve for its counterimage at Lev 16B's position. Replacing 1% (panel **a**), 3% (panel **b**), and 10% (panel **c**) of smooth DM with 30 $M_\odot$ BHs yields light curves where the average magnification varies on an increasingly long timescales. An extended period of low magnification for one of the pair of images could help to explain why only a single image, LS1 / Lev16A, is persistently visible in *HST* imaging.

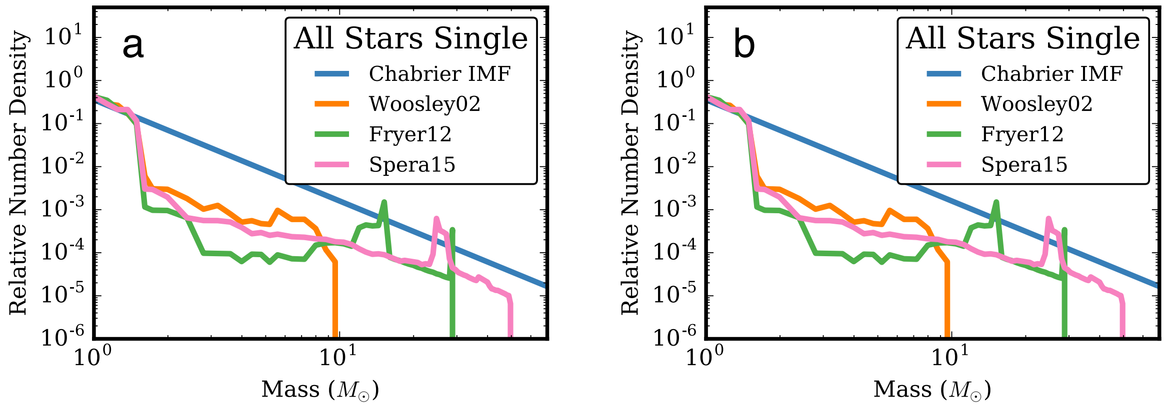


Supplementary Figure 12: **Differences among the mass distributions of surviving stars and stellar remnants (i.e., white dwarf stars, neutron stars, and BHs) for the Woosley02 (orange line), Fryer12 (green line), and Spera15 (magenta line) stellar evolution models.** Blue line shows the mass function corresponding to a Chabrier IMF. **a,** The mass distributions assuming no stars have companions. **b,** Mass functions assuming the mass-dependent binary fractions and mass ratios measured in the nearby universe[31].

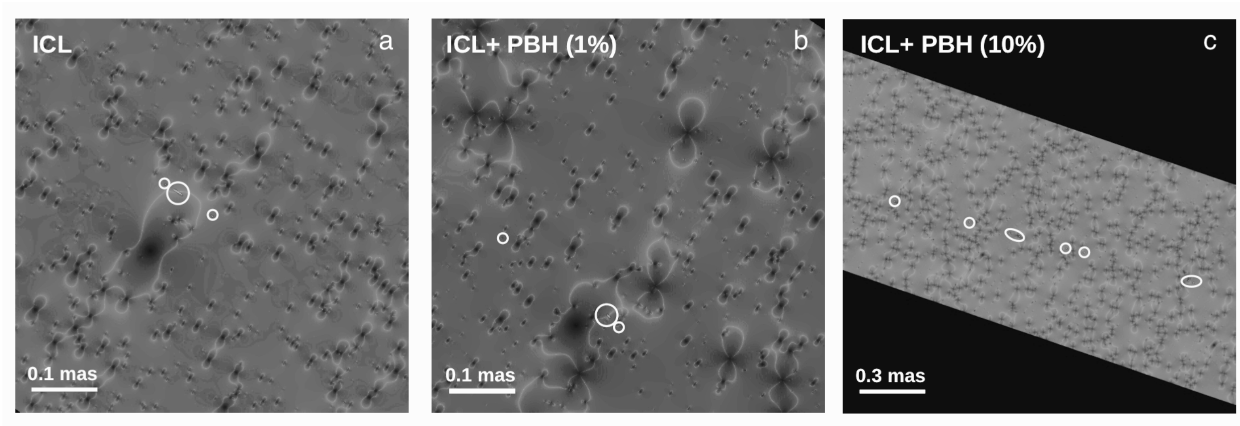


Supplementary Figure 13: **Examples of trains of multiple counterimages of a single background star as it traverses the region near the galaxy-cluster caustic.** In general, there is a single counterimage per microlens[35], but most images have magnifications of order unity or even less and are not detectable. **a,** A train from a simulation where the cluster lens contains no PBHs. **b,** A train from a simulation where $30\,M_\odot$ PBHs account for 1% of DM. **c,** A train from a simulation where $30\,M_\odot$ PBHs account for 10% of DM in panel. Increasing the PBH abundance yields more extended trains, although their extent ($\sim 3$ milliarcsec) when PBHs account for 10% would be too small to detect in *HST* imaging. The simulation shown is of a $1000\,R_\odot$ star whose image appears at an offset of $0.13''$ from the cluster critical curve. Near peak magnification, the star appears as a "train" of counterimages. Each circle in panel **c** encloses one image, and each ellipse encloses a set of two or three closely spaced images, in the train. The sizes of the circles and ellipses indicate the magnification of each image or set of images, respectively. In addition to replacing fractions of cluster DM with PBHs, we have populated the lens plane with stars and compact object remnants to match the mass density in surviving stars and remnants we infer for the ICM ($1.1^{+0.3}_{-0.3} \times 10^7\,M_\odot\,\mathrm{kpc}^{-2}$).

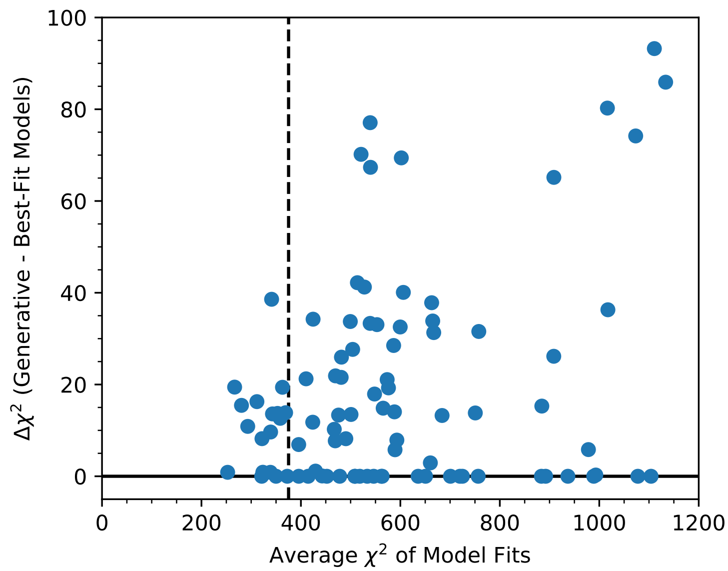


Supplementary Figure 14: **Confidence intervals for $\langle\chi^2\rangle$ statistics determined using simulated light curves.** For the models listed in Table 1, we generate simulated light curves for stars with $M_V = \{-8, -9, -10\}$, and fit them, allowing the lensed star to have an absolute magnitude within the range $-7.5 < M_V < -9.5$. The dashed black vertical shows the average of the $\langle\chi^2\rangle$ statistics for the Table 1 models for LS 1/ Lev16A and Lev16B. For all simulated light curves where the average $\langle\chi^2\rangle$ value is within 100 of the vertical dashed line, we calculate the difference $\Delta\langle\chi^2\rangle$ values between the $\langle\chi^2\rangle$ values of the generative ("true") model and of the best-fitting model. For 68% of simulated light curves, $\Delta\langle\chi^2\rangle \lesssim 13$, and, for 95% of simulated light curves, $\Delta\langle\chi^2\rangle \lesssim 25$. The horizontal black line plots $\Delta\langle\chi^2\rangle = 0$.

| Date (MJD) | Bandpass | Flux | $\sigma$ |
|---|---|---|---|
| 57538.38 | ACS F275W | -0.160 | 0.192 |
| 57531.29 | ACS F336W | 0.348 | 0.242 |
| 57538.33 | ACS F336W | 0.394 | 0.226 |
| 57531.37 | ACS F475W | -0.005 | 0.098 |
| 57531.46 | ACS F435W | -0.303 | 0.162 |
| 57531.46 | ACS F435W | -0.033 | 0.184 |
| 57524.28 | ACS F606W | 0.295 | 0.055 |
| 57524.28 | ACS F606W | 0.329 | 0.044 |
| 57531.71 | ACS F606W | 0.332 | 0.076 |
| 57531.71 | ACS F606W | 0.438 | 0.054 |
| 57534.29 | ACS F606W | 0.446 | 0.095 |
| 57534.29 | ACS F606W | 0.522 | 0.063 |
| 57536.10 | ACS F606W | 0.422 | 0.098 |
| 57536.10 | ACS F606W | 0.470 | 0.068 |
| 57537.09 | ACS F606W | 0.555 | 0.086 |
| 57537.09 | ACS F606W | 0.588 | 0.070 |
| 57524.38 | ACS F814W | 0.231 | 0.058 |
| 57524.38 | ACS F814W | 0.304 | 0.038 |
| 57531.49 | ACS F814W | 0.164 | 0.094 |
| 57531.49 | ACS F814W | 0.189 | 0.062 |
| 57524.47 | WFC3 F105W | 0.528 | 0.113 |
| 57524.47 | WFC3 F105W | 0.681 | 0.095 |
| 57524.47 | WFC3 F125W | 0.510 | 0.125 |
| 57524.47 | WFC3 F125W | 0.624 | 0.097 |
| 57524.61 | WFC3 F125W | 0.578 | 0.092 |
| 57524.61 | WFC3 F125W | 0.669 | 0.085 |
| 57527.18 | WFC3 F125W | 0.608 | 0.142 |
| 57527.18 | WFC3 F125W | 0.748 | 0.122 |
| 57532.02 | WFC3 F125W | 0.556 | 0.145 |
| 57532.02 | WFC3 F125W | 0.696 | 0.138 |
| 57534.27 | WFC3 F125W | 0.967 | 0.141 |
| 57534.27 | WFC3 F125W | 1.174 | 0.129 |
| 57536.06 | WFC3 F125W | 1.015 | 0.140 |
| 57536.06 | WFC3 F125W | 1.211 | 0.124 |
| 57537.05 | WFC3 F125W | 1.022 | 0.134 |
| 57537.05 | WFC3 F125W | 1.216 | 0.128 |
| 57538.31 | WFC3 F125W | 0.930 | 0.148 |
| 57538.31 | WFC3 F125W | 1.154 | 0.121 |
| 57524.54 | WFC3 F160W | 0.381 | 0.110 |
| 57524.54 | WFC3 F160W | 0.489 | 0.093 |
| 57527.20 | WFC3 F160W | 0.320 | 0.153 |

| Date (MJD) | Bandpass | Flux | $\sigma$ |
|---|---|---|---|
| 57527.20 | WFC3 F160W | 0.427 | 0.155 |

Supplementary Table 1: **Flux at LS1's position during Lev16A after subtracting flux present in 2011 imaging.** Fluxes are measured from difference images created by subtracting exposures acquired in 2016 from template images taken in 2011. The zeropoint of listed fluxes is 25 AB, and no correction for Galactic extinction is applied.

| Bandpass | Flux | $\sigma$ |
|---|---|---|
| ACS $F225W$ | -0.007 | 0.026 |
| ACS $F275W$ | -0.005 | 0.019 |
| ACS $F336W$ | 0.019 | 0.010 |
| ACS $F435W$ | 0.024 | 0.005 |
| ACS $F606W$ | 0.050 | 0.006 |
| ACS $F814W$ | 0.072 | 0.003 |
| WFC3 $F105W$ | 0.143 | 0.006 |
| WFC3 $F125W$ | 0.141 | 0.008 |
| WFC3 $F140W$ | 0.113 | 0.004 |
| WFC3 $F160W$ | 0.127 | 0.011 |

Supplementary Table 2: **Photometry of LS1 measured from HFF imaging (2013–2014), and archival near-UV *HST* imaging.** The zeropoint of listed fluxes is 25 AB, and a correction for Galactic extinction is applied.

| Bandpass | Flux | $\sigma$ |
|---|---|---|
| ACS $F225W$ | −0.329 | 0.011 |
| ACS $F275W$ | 0.110 | 0.054 |
| ACS $F336W$ | 0.100 | 0.027 |
| ACS $F435W$ | 0.089 | 0.016 |
| ACS $F606W$ | 0.098 | 0.014 |
| ACS $F814W$ | 0.091 | 0.008 |
| WFC3 $F105W$ | 0.095 | 0.008 |
| WFC3 $F125W$ | 0.097 | 0.009 |
| WFC3 $F140W$ | 0.097 | 0.011 |
| WFC3 $F160W$ | 0.107 | 0.010 |

Supplementary Table 3: **Photometry of underlying lensed arc adjacent to LS1.** The zeropoint of listed fluxes is 25 AB, and fluxes are corrected for Galactic extinction.

| Date (MJD) | Bandpass | LS1/2016A | | 2016B | | 2017A | |
|---|---|---|---|---|---|---|---|
| | | Flux | $\sigma$ | Flux | $\sigma$ | Flux | $\sigma$ |
| 55534.98 | WFC3 F125W | 0.079 [0.079] | 0.040 [0.040] | 0.019 | 0.055 | 0.021 | 0.044 |
| 55629.90 | WFC3 F125W | 0.106 [0.106] | 0.045 [0.045] | -0.028 | 0.057 | 0.008 | 0.050 |
| 56981.06 | WFC3 F125W | 0.148 [0.148] | 0.019 [0.019] | -0.009 | 0.014 | -0.014 | 0.017 |
| 56982.12 | WFC3 F125W | 0.125 [0.125] | 0.020 [0.020] | -0.016 | 0.018 | -0.020 | 0.017 |
| 56983.04 | WFC3 F125W | 0.131 [0.131] | 0.019 [0.019] | -0.017 | 0.018 | 0.006 | 0.014 |
| 56983.31 | WFC3 F125W | 0.112 [0.112] | 0.014 [0.014] | -0.013 | 0.019 | -0.006 | 0.016 |
| 56990.90 | WFC3 F125W | 0.198 [0.198] | 0.046 [0.046] | -0.038 | 0.055 | -0.017 | 0.056 |
| 56992.95 | WFC3 F125W | 0.130 [0.130] | 0.059 [0.059] | -0.044 | 0.038 | -0.024 | 0.042 |
| 56994.01 | WFC3 F125W | 0.146 [0.146] | 0.033 [0.033] | -0.029 | 0.047 | -0.045 | 0.051 |
| 56996.73 | WFC3 F125W | 0.149 [0.149] | 0.045 [0.045] | 0.012 | 0.072 | -0.016 | 0.061 |
| 56999.52 | WFC3 F125W | 0.150 [0.150] | 0.044 [0.044] | -0.028 | 0.049 | 0.015 | 0.044 |
| 57000.11 | WFC3 F125W | 0.096 [0.096] | 0.073 [0.073] | 0.068 | 0.063 | 0.038 | 0.042 |
| 57005.86 | WFC3 F125W | 0.148 [0.148] | 0.021 [0.021] | 0.012 | 0.016 | 0.005 | 0.012 |
| 57019.94 | WFC3 F125W | 0.061 [0.061] | 0.076 [0.076] | -0.174 | 0.104 | -0.075 | 0.112 |
| 57020.80 | WFC3 F125W | 0.006 [0.006] | 0.099 [0.099] | 0.005 | 0.088 | 0.080 | 0.079 |
| 57021.80 | WFC3 F125W | 0.126 [0.126] | 0.093 [0.093] | 0.042 | 0.103 | -0.026 | 0.102 |
| 57024.72 | WFC3 F125W | 0.100 [0.100] | 0.102 [0.102] | 0.058 | 0.119 | 0.010 | 0.044 |
| 57025.78 | WFC3 F125W | 0.094 [0.094] | 0.082 [0.082] | -0.069 | 0.115 | -0.012 | 0.072 |
| 57025.91 | WFC3 F125W | 0.055 [0.055] | 0.089 [0.089] | 0.034 | 0.104 | -0.007 | 0.098 |
| 57026.90 | WFC3 F125W | 0.018 [0.018] | 0.080 [0.080] | -0.087 | 0.133 | -0.109 | 0.082 |
| 57029.54 | WFC3 F125W | 0.151 [0.151] | 0.016 [0.016] | 0.037 | 0.015 | 0.029 | 0.014 |
| 57033.94 | WFC3 F125W | 0.144 [0.144] | 0.044 [0.044] | -0.043 | 0.043 | -0.002 | 0.046 |
| 57036.60 | WFC3 F125W | 0.109 [0.109] | 0.046 [0.046] | 0.010 | 0.050 | 0.045 | 0.041 |
| 57044.69 | WFC3 F125W | 0.120 [0.120] | 0.036 [0.036] | 0.029 | 0.040 | 0.011 | 0.040 |
| 57049.20 | WFC3 F125W | 0.099 [0.099] | 0.033 [0.033] | -0.006 | 0.030 | 0.023 | 0.039 |
| 57062.36 | WFC3 F125W | 0.120 [0.120] | 0.040 [0.040] | 0.041 | 0.046 | 0.041 | 0.047 |
| 57076.39 | WFC3 F125W | 0.111 [0.111] | 0.039 [0.039] | 0.001 | 0.055 | -0.011 | 0.047 |
| 57090.39 | WFC3 F125W | 0.103 [0.103] | 0.037 [0.037] | -0.033 | 0.031 | -0.032 | 0.052 |
| 57104.27 | WFC3 F125W | 0.132 [0.132] | 0.057 [0.057] | -0.017 | 0.050 | -0.028 | 0.045 |
| 57118.14 | WFC3 F125W | 0.110 [0.110] | 0.040 [0.040] | -0.002 | 0.042 | -0.016 | 0.044 |
| 57132.09 | WFC3 F125W | 0.144 [0.144] | 0.068 [0.068] | -0.027 | 0.071 | 0.001 | 0.079 |
| 57149.06 | WFC3 F125W | 0.079 [0.079] | 0.055 [0.055] | 0.058 | 0.045 | 0.047 | 0.076 |
| 57188.17 | WFC3 F125W | 0.148 [0.148] | 0.040 [0.040] | 0.004 | 0.049 | 0.009 | 0.031 |
| 57216.20 | WFC3 F125W | 0.153 [0.153] | 0.049 [0.049] | -0.062 | 0.050 | 0.010 | 0.039 |
| 57223.96 | WFC3 F125W | 0.095 [0.095] | 0.054 [0.054] | 0.030 | 0.044 | 0.033 | 0.044 |
| 57325.82 | WFC3 F125W | 0.044 [0.044] | 0.060 [0.060] | -0.023 | 0.077 | 0.005 | 0.049 |
| 57340.94 | WFC3 F125W | 0.109 [0.109] | 0.035 [0.035] | 0.039 | 0.043 | 0.026 | 0.050 |
| 57367.04 | WFC3 F125W | 0.131 [0.131] | 0.051 [0.051] | 0.071 | 0.053 | 0.053 | 0.051 |
| 57402.11 | WFC3 F125W | 0.212 [0.212] | 0.045 [0.045] | -0.027 | 0.034 | 0.011 | 0.039 |
| 57426.21 | WFC3 F125W | 0.155 [0.155] | 0.037 [0.037] | 0.007 | 0.037 | -0.012 | 0.044 |
| 57430.59 | WFC3 F125W | 0.195 [0.195] | 0.046 [0.046] | 0.024 | 0.038 | 0.049 | 0.037 |

| Date (MJD) | Bandpass | LS1/2016A Flux | LS1/2016A σ | 2016B Flux | 2016B σ | 2017A Flux | 2017A σ |
|---|---|---|---|---|---|---|---|
| 57444.57 | WFC3 F125W | 0.174 [0.174] | 0.033 [0.033] | 0.008 | 0.029 | -0.024 | 0.044 |
| 57459.03 | WFC3 F125W | 0.243 [0.243] | 0.056 [0.056] | 0.107 | 0.046 | 0.063 | 0.057 |
| 57472.53 | WFC3 F125W | 0.251 [0.251] | 0.049 [0.049] | 0.051 | 0.044 | 0.106 | 0.041 |
| 57493.26 | WFC3 F125W | 0.323 [0.323] | 0.048 [0.048] | 0.018 | 0.044 | 0.072 | 0.041 |
| 57507.53 | WFC3 F125W | 0.462 [0.462] | 0.033 [0.033] | -0.031 | 0.030 | 0.005 | 0.042 |
| 57521.27 | WFC3 F125W | 0.328 [0.328] | 0.055 [0.055] | 0.010 | 0.036 | -0.047 | 0.052 |
| 57524.47 | WFC3 F125W | 0.313 [0.313] | 0.056 [0.056] | -0.027 | 0.041 | 0.016 | 0.044 |
| 57524.60 | WFC3 F125W | 0.399 [0.399] | 0.045 [0.045] | -0.020 | 0.044 | -0.013 | 0.049 |
| 57524.61 | WFC3 F125W | 0.280 [0.280] | 0.041 [0.041] | -0.021 | 0.039 | 0.000 | 0.038 |
| 57527.18 | WFC3 F125W | 0.345 [0.345] | 0.038 [0.038] | 0.010 | 0.046 | 0.031 | 0.044 |
| 57532.02 | WFC3 F125W | 0.326 [0.326] | 0.048 [0.048] | 0.033 | 0.063 | 0.072 | 0.060 |
| 57534.27 | WFC3 F125W | 0.563 [0.563] | 0.068 [0.068] | 0.001 | 0.071 | 0.027 | 0.056 |
| 57536.06 | WFC3 F125W | 0.517 [0.517] | 0.064 [0.064] | -0.020 | 0.054 | 0.038 | 0.060 |
| 57537.05 | WFC3 F125W | 0.516 [0.516] | 0.051 [0.051] | 0.051 | 0.054 | 0.039 | 0.048 |
| 57538.31 | WFC3 F125W | 0.489 [0.489] | 0.066 [0.066] | 0.043 | 0.052 | 0.060 | 0.044 |
| 57541.09 | WFC3 F125W | 0.233 [0.233] | 0.042 [0.042] | 0.068 | 0.028 | -0.011 | 0.049 |
| 57545.07 | WFC3 F125W | 0.286 [0.286] | 0.071 [0.071] | -0.005 | 0.071 | 0.019 | 0.055 |
| 57547.05 | WFC3 F125W | 0.214 [0.214] | 0.057 [0.057] | -0.002 | 0.049 | -0.004 | 0.048 |
| 57549.00 | WFC3 F125W | 0.161 [0.161] | 0.062 [0.062] | 0.036 | 0.070 | -0.013 | 0.047 |
| 57550.04 | WFC3 F125W | 0.141 [0.141] | 0.057 [0.057] | -0.034 | 0.063 | -0.019 | 0.035 |
| 57551.67 | WFC3 F125W | 0.130 [0.130] | 0.071 [0.071] | 0.022 | 0.042 | 0.048 | 0.054 |
| 57553.73 | WFC3 F125W | 0.204 [0.204] | 0.071 [0.071] | 0.018 | 0.087 | 0.023 | 0.053 |
| 57555.91 | WFC3 F125W | 0.182 [0.182] | 0.044 [0.044] | -0.040 | 0.057 | 0.017 | 0.057 |
| 57557.50 | WFC3 F125W | 0.100 [0.100] | 0.069 [0.069] | -0.007 | 0.056 | -0.042 | 0.055 |
| 57566.20 | WFC3 F125W | 0.159 [0.159] | 0.055 [0.055] | 0.006 | 0.053 | 0.006 | 0.051 |
| 57569.25 | WFC3 F125W | 0.181 [0.181] | 0.055 [0.055] | -0.070 | 0.047 | -0.051 | 0.026 |
| 57573.22 | WFC3 F125W | 0.146 [0.146] | 0.041 [0.041] | 0.090 | 0.046 | 0.072 | 0.046 |
| 57577.71 | WFC3 F125W | 0.170 [0.170] | 0.043 [0.043] | -0.011 | 0.053 | 0.017 | 0.034 |
| 57580.18 | WFC3 F125W | 0.177 [0.177] | 0.053 [0.053] | 0.067 | 0.059 | 0.053 | 0.066 |
| 57583.09 | WFC3 F125W | 0.168 [0.168] | 0.068 [0.068] | -0.039 | 0.072 | 0.017 | 0.072 |
| 57586.01 | WFC3 F125W | 0.252 [0.252] | 0.060 [0.060] | 0.069 | 0.045 | 0.031 | 0.054 |
| 57589.19 | WFC3 F125W | 0.232 [0.232] | 0.058 [0.058] | -0.053 | 0.059 | -0.047 | 0.060 |
| 57592.04 | WFC3 F125W | 0.111 [0.111] | 0.071 [0.071] | 0.055 | 0.056 | 0.034 | 0.059 |
| 57691.20 | WFC3 F125W | 0.257 [0.257] | 0.055 [0.055] | 0.391 | 0.055 | 0.260 | 0.040 |
| 57720.81 | WFC3 F125W | 0.103 [0.103] | 0.038 [0.038] | 0.008 | 0.041 | 0.006 | 0.023 |
| 57727.04 | WFC3 F125W | 0.155 [0.155] | 0.038 [0.038] | -0.001 | 0.038 | 0.046 | 0.046 |
| 57756.90 | WFC3 F125W | 0.159 [0.159] | 0.037 [0.037] | 0.083 | 0.033 | 0.147 | 0.029 |
| 55591.70 | WFC3 F105W | 0.031 [0.032] | 0.035 [0.037] | 0.009 | 0.032 | 0.011 | 0.028 |
| 55619.67 | WFC3 F105W | 0.139 [0.145] | 0.045 [0.048] | 0.014 | 0.036 | -0.021 | 0.040 |
| 56711.48 | WFC3 F105W | 0.297 [0.311] | 0.063 [0.067] | 0.011 | 0.068 | 0.018 | 0.065 |
| 56711.94 | WFC3 F105W | 0.279 [0.291] | 0.094 [0.100] | -0.044 | 0.059 | -0.007 | 0.088 |

| Date (MJD) | Bandpass | LS1/2016A Flux | LS1/2016A $\sigma$ | 2016B Flux | 2016B $\sigma$ | 2017A Flux | 2017A $\sigma$ |
|---|---|---|---|---|---|---|---|
| 56713.63 | WFC3 F105W | 0.260 [0.272] | 0.088 [0.094] | 0.004 | 0.071 | -0.052 | 0.077 |
| 56964.16 | WFC3 F105W | 0.180 [0.188] | 0.078 [0.083] | 0.000 | 0.062 | -0.095 | 0.078 |
| 56968.88 | WFC3 F105W | 0.138 [0.145] | 0.134 [0.143] | -0.091 | 0.105 | 0.034 | 0.106 |
| 56972.06 | WFC3 F105W | 0.207 [0.217] | 0.107 [0.114] | 0.077 | 0.137 | 0.172 | 0.138 |
| 56982.31 | WFC3 F105W | 0.109 [0.114] | 0.028 [0.029] | -0.014 | 0.032 | -0.004 | 0.029 |
| 57002.87 | WFC3 F105W | 0.137 [0.143] | 0.014 [0.015] | 0.000 | 0.018 | -0.014 | 0.017 |
| 57006.98 | WFC3 F105W | 0.134 [0.140] | 0.016 [0.017] | 0.003 | 0.015 | 0.017 | 0.019 |
| 57011.89 | WFC3 F105W | 0.123 [0.129] | 0.015 [0.016] | -0.000 | 0.013 | 0.005 | 0.019 |
| 57014.88 | WFC3 F105W | 0.157 [0.164] | 0.015 [0.016] | 0.014 | 0.019 | 0.009 | 0.018 |
| 57015.81 | WFC3 F105W | 0.090 [0.094] | 0.016 [0.017] | 0.006 | 0.015 | -0.008 | 0.009 |
| 57017.80 | WFC3 F105W | 0.126 [0.132] | 0.014 [0.015] | 0.000 | 0.017 | 0.002 | 0.014 |
| 57020.58 | WFC3 F105W | 0.125 [0.130] | 0.013 [0.014] | -0.027 | 0.012 | -0.012 | 0.013 |
| 57023.77 | WFC3 F105W | 0.135 [0.141] | 0.016 [0.017] | 0.015 | 0.016 | 0.014 | 0.014 |
| 57025.56 | WFC3 F105W | 0.119 [0.125] | 0.012 [0.013] | -0.013 | 0.013 | -0.001 | 0.015 |
| 57026.49 | WFC3 F105W | 0.139 [0.146] | 0.013 [0.014] | -0.015 | 0.012 | -0.016 | 0.016 |
| 57027.81 | WFC3 F105W | 0.123 [0.128] | 0.014 [0.015] | 0.023 | 0.010 | 0.008 | 0.009 |
| 57132.10 | WFC3 F105W | 0.118 [0.124] | 0.064 [0.068] | -0.014 | 0.069 | 0.008 | 0.061 |
| 57149.07 | WFC3 F105W | 0.138 [0.145] | 0.048 [0.051] | 0.046 | 0.067 | 0.022 | 0.057 |
| 57168.28 | WFC3 F105W | 0.070 [0.073] | 0.019 [0.021] | 0.012 | 0.022 | -0.006 | 0.034 |
| 57208.06 | WFC3 F105W | 0.068 [0.071] | 0.054 [0.057] | -0.047 | 0.033 | 0.004 | 0.047 |
| 57216.28 | WFC3 F105W | 0.129 [0.135] | 0.043 [0.046] | -0.029 | 0.042 | -0.000 | 0.034 |
| 57430.59 | WFC3 F105W | 0.183 [0.192] | 0.030 [0.032] | 0.005 | 0.019 | -0.023 | 0.024 |
| 57432.75 | WFC3 F105W | 0.157 [0.164] | 0.023 [0.025] | 0.042 | 0.019 | 0.028 | 0.022 |
| 57524.47 | WFC3 F105W | 0.367 [0.384] | 0.031 [0.033] | 0.005 | 0.035 | -0.002 | 0.025 |
| 55535.00 | WFC3 F160W | 0.000 [0.000] | 0.078 [0.100] | -0.005 | 0.072 | -0.042 | 0.068 |
| 55577.06 | WFC3 F160W | 0.062 [0.078] | 0.063 [0.082] | 0.004 | 0.059 | -0.003 | 0.058 |
| 55619.12 | WFC3 F160W | 0.099 [0.125] | 0.059 [0.076] | -0.052 | 0.062 | -0.057 | 0.061 |
| 55629.85 | WFC3 F160W | 0.116 [0.146] | 0.058 [0.075] | -0.035 | 0.052 | -0.036 | 0.063 |
| 56598.14 | WFC3 F160W | 0.061 [0.077] | 0.026 [0.033] | -0.010 | 0.027 | -0.010 | 0.035 |
| 56990.91 | WFC3 F160W | 0.126 [0.159] | 0.086 [0.111] | -0.067 | 0.087 | -0.104 | 0.088 |
| 56992.97 | WFC3 F160W | 0.038 [0.048] | 0.096 [0.124] | 0.002 | 0.048 | -0.004 | 0.108 |
| 56994.03 | WFC3 F160W | 0.076 [0.095] | 0.033 [0.042] | -0.016 | 0.066 | 0.041 | 0.061 |
| 56996.75 | WFC3 F160W | 0.075 [0.094] | 0.058 [0.075] | -0.086 | 0.113 | -0.080 | 0.106 |
| 56999.56 | WFC3 F160W | 0.048 [0.060] | 0.067 [0.087] | 0.052 | 0.085 | 0.036 | 0.083 |
| 57000.13 | WFC3 F160W | 0.146 [0.185] | 0.061 [0.079] | 0.057 | 0.081 | -0.048 | 0.081 |
| 57002.89 | WFC3 F160W | 0.118 [0.149] | 0.022 [0.028] | 0.002 | 0.023 | -0.003 | 0.019 |
| 57007.00 | WFC3 F160W | 0.111 [0.140] | 0.023 [0.030] | -0.021 | 0.019 | -0.011 | 0.014 |
| 57011.91 | WFC3 F160W | 0.124 [0.157] | 0.023 [0.030] | 0.032 | 0.023 | 0.008 | 0.027 |
| 57014.87 | WFC3 F160W | 0.020 [0.025] | 0.026 [0.034] | 0.005 | 0.031 | 0.025 | 0.027 |
| 57015.82 | WFC3 F160W | 0.124 [0.157] | 0.025 [0.032] | 0.014 | 0.023 | 0.015 | 0.021 |
| 57016.79 | WFC3 F160W | 0.072 [0.091] | 0.057 [0.074] | 0.069 | 0.089 | -0.034 | 0.108 |

| Date | Bandpass | LS1/2016A | | 2016B | | 2017A | |
|---|---|---|---|---|---|---|---|
| (MJD) | | Flux | $\sigma$ | Flux | $\sigma$ | Flux | $\sigma$ |
| 57017.82 | WFC3 F160W | 0.097 [0.122] | 0.017 [0.022] | 0.006 | 0.017 | -0.008 | 0.019 |
| 57018.78 | WFC3 F160W | 0.076 [0.096] | 0.099 [0.128] | 0.073 | 0.084 | 0.041 | 0.105 |
| 57019.64 | WFC3 F160W | -0.082 [-0.103] | 0.094 [0.121] | -0.196 | 0.164 | -0.048 | 0.128 |
| 57020.60 | WFC3 F160W | 0.187 [0.236] | 0.028 [0.037] | -0.014 | 0.028 | -0.028 | 0.028 |
| 57020.94 | WFC3 F160W | -0.004 [-0.006] | 0.143 [0.185] | 0.230 | 0.134 | 0.160 | 0.166 |
| 57023.78 | WFC3 F160W | 0.085 [0.107] | 0.020 [0.026] | 0.008 | 0.020 | 0.012 | 0.025 |
| 57025.57 | WFC3 F160W | 0.108 [0.136] | 0.023 [0.029] | -0.007 | 0.013 | -0.013 | 0.023 |
| 57026.50 | WFC3 F160W | 0.116 [0.147] | 0.020 [0.026] | -0.019 | 0.027 | 0.002 | 0.021 |
| 57027.83 | WFC3 F160W | 0.114 [0.143] | 0.025 [0.032] | 0.004 | 0.026 | 0.008 | 0.019 |
| 57033.96 | WFC3 F160W | 0.116 [0.147] | 0.067 [0.086] | -0.083 | 0.050 | -0.072 | 0.053 |
| 57036.61 | WFC3 F160W | 0.082 [0.103] | 0.039 [0.051] | -0.012 | 0.061 | -0.092 | 0.048 |
| 57044.71 | WFC3 F160W | 0.102 [0.129] | 0.057 [0.074] | 0.038 | 0.058 | 0.067 | 0.063 |
| 57049.21 | WFC3 F160W | 0.108 [0.136] | 0.034 [0.044] | 0.034 | 0.048 | 0.007 | 0.047 |
| 57062.40 | WFC3 F160W | 0.077 [0.097] | 0.074 [0.096] | -0.002 | 0.061 | -0.036 | 0.073 |
| 57076.41 | WFC3 F160W | 0.117 [0.147] | 0.065 [0.083] | 0.030 | 0.071 | 0.025 | 0.067 |
| 57090.42 | WFC3 F160W | 0.149 [0.188] | 0.074 [0.096] | 0.056 | 0.053 | -0.028 | 0.060 |
| 57104.31 | WFC3 F160W | 0.072 [0.091] | 0.070 [0.091] | 0.027 | 0.080 | -0.017 | 0.079 |
| 57118.22 | WFC3 F160W | 0.091 [0.115] | 0.074 [0.096] | 0.014 | 0.072 | -0.015 | 0.074 |
| 57132.11 | WFC3 F160W | 0.029 [0.036] | 0.067 [0.086] | 0.001 | 0.081 | 0.065 | 0.091 |
| 57149.08 | WFC3 F160W | 0.127 [0.161] | 0.086 [0.112] | 0.051 | 0.077 | -0.027 | 0.086 |
| 57168.29 | WFC3 F160W | 0.059 [0.074] | 0.066 [0.085] | 0.026 | 0.057 | 0.021 | 0.089 |
| 57188.19 | WFC3 F160W | 0.035 [0.045] | 0.096 [0.123] | -0.126 | 0.095 | -0.057 | 0.087 |
| 57208.09 | WFC3 F160W | 0.094 [0.119] | 0.088 [0.113] | -0.069 | 0.094 | 0.002 | 0.079 |
| 57216.22 | WFC3 F160W | 0.109 [0.138] | 0.052 [0.067] | -0.137 | 0.079 | -0.072 | 0.055 |
| 57224.00 | WFC3 F160W | 0.019 [0.024] | 0.062 [0.080] | 0.036 | 0.070 | 0.053 | 0.072 |
| 57325.84 | WFC3 F160W | 0.085 [0.108] | 0.064 [0.083] | -0.014 | 0.081 | -0.078 | 0.059 |
| 57340.95 | WFC3 F160W | 0.125 [0.158] | 0.081 [0.105] | -0.044 | 0.058 | -0.011 | 0.047 |
| 57367.06 | WFC3 F160W | 0.082 [0.104] | 0.075 [0.097] | 0.009 | 0.062 | -0.055 | 0.052 |
| 57402.15 | WFC3 F160W | 0.155 [0.196] | 0.061 [0.078] | 0.044 | 0.061 | 0.013 | 0.033 |
| 57426.23 | WFC3 F160W | 0.157 [0.198] | 0.071 [0.092] | 0.083 | 0.055 | 0.043 | 0.062 |
| 57432.75 | WFC3 F160W | 0.147 [0.185] | 0.046 [0.059] | -0.074 | 0.042 | -0.015 | 0.052 |
| 57444.61 | WFC3 F160W | 0.084 [0.106] | 0.059 [0.076] | -0.090 | 0.045 | -0.064 | 0.054 |
| 57459.09 | WFC3 F160W | 0.237 [0.299] | 0.056 [0.072] | 0.023 | 0.059 | -0.032 | 0.036 |
| 57472.54 | WFC3 F160W | 0.166 [0.210] | 0.064 [0.083] | 0.102 | 0.068 | 0.088 | 0.030 |
| 57493.30 | WFC3 F160W | 0.229 [0.289] | 0.070 [0.090] | 0.079 | 0.069 | 0.094 | 0.074 |
| 57507.57 | WFC3 F160W | 0.269 [0.339] | 0.062 [0.080] | 0.094 | 0.067 | 0.088 | 0.069 |
| 57521.30 | WFC3 F160W | 0.253 [0.319] | 0.060 [0.077] | 0.071 | 0.055 | 0.089 | 0.063 |
| 57524.54 | WFC3 F160W | 0.259 [0.327] | 0.047 [0.061] | -0.020 | 0.043 | 0.038 | 0.035 |
| 57527.20 | WFC3 F160W | 0.244 [0.309] | 0.053 [0.069] | -0.018 | 0.058 | 0.037 | 0.064 |
| 57541.13 | WFC3 F160W | 0.168 [0.212] | 0.054 [0.070] | -0.021 | 0.062 | -0.030 | 0.070 |
| 57545.10 | WFC3 F160W | 0.301 [0.380] | 0.081 [0.105] | -0.070 | 0.055 | -0.022 | 0.075 |

| Date (MJD) | Bandpass | LS1/2016A Flux | LS1/2016A $\sigma$ | 2016B Flux | 2016B $\sigma$ | 2017A Flux | 2017A $\sigma$ |
|---|---|---|---|---|---|---|---|
| 57547.09 | WFC3 F160W | 0.212 [0.268] | 0.075 [0.097] | -0.006 | 0.061 | 0.003 | 0.078 |
| 57549.04 | WFC3 F160W | 0.139 [0.176] | 0.060 [0.077] | 0.009 | 0.075 | -0.029 | 0.071 |
| 57550.10 | WFC3 F160W | 0.104 [0.131] | 0.077 [0.099] | -0.102 | 0.089 | -0.062 | 0.092 |
| 57551.71 | WFC3 F160W | 0.176 [0.222] | 0.076 [0.098] | -0.103 | 0.071 | -0.084 | 0.068 |
| 57553.79 | WFC3 F160W | 0.121 [0.153] | 0.107 [0.138] | -0.096 | 0.106 | -0.053 | 0.083 |
| 57555.95 | WFC3 F160W | 0.188 [0.237] | 0.087 [0.112] | -0.010 | 0.091 | 0.011 | 0.078 |
| 57557.53 | WFC3 F160W | 0.139 [0.175] | 0.043 [0.056] | -0.011 | 0.055 | -0.069 | 0.098 |
| 57566.22 | WFC3 F160W | 0.169 [0.214] | 0.079 [0.103] | -0.074 | 0.066 | -0.072 | 0.052 |
| 57569.26 | WFC3 F160W | 0.133 [0.168] | 0.067 [0.086] | -0.093 | 0.081 | -0.085 | 0.082 |
| 57573.24 | WFC3 F160W | 0.155 [0.196] | 0.051 [0.066] | -0.036 | 0.077 | -0.021 | 0.047 |
| 57577.74 | WFC3 F160W | 0.226 [0.286] | 0.077 [0.100] | -0.038 | 0.073 | 0.010 | 0.069 |
| 57583.13 | WFC3 F160W | 0.163 [0.206] | 0.079 [0.102] | -0.066 | 0.073 | 0.032 | 0.060 |
| 57586.05 | WFC3 F160W | -0.005 [-0.006] | 0.068 [0.088] | 0.059 | 0.113 | -0.038 | 0.064 |
| 57589.20 | WFC3 F160W | 0.018 [0.023] | 0.073 [0.094] | -0.135 | 0.069 | -0.061 | 0.063 |
| 57691.21 | WFC3 F160W | 0.207 [0.261] | 0.088 [0.113] | 0.352 | 0.088 | 0.258 | 0.065 |
| 57727.07 | WFC3 F160W | 0.112 [0.142] | 0.056 [0.072] | -0.053 | 0.077 | 0.016 | 0.070 |
| 55591.71 | WFC3 F140W | 0.072 [0.092] | 0.043 [0.054] | 0.016 | 0.040 | -0.026 | 0.030 |
| 55619.65 | WFC3 F140W | 0.009 [0.011] | 0.038 [0.047] | -0.002 | 0.043 | -0.013 | 0.045 |
| 56711.77 | WFC3 F140W | 0.208 [0.265] | 0.071 [0.090] | 0.022 | 0.063 | 0.048 | 0.056 |
| 56971.93 | WFC3 F140W | 0.160 [0.204] | 0.059 [0.074] | -0.111 | 0.069 | -0.101 | 0.081 |
| 56972.13 | WFC3 F140W | 0.261 [0.332] | 0.080 [0.100] | 0.109 | 0.081 | 0.107 | 0.109 |
| 56981.85 | WFC3 F140W | 0.084 [0.107] | 0.016 [0.020] | 0.001 | 0.019 | -0.004 | 0.016 |
| 56981.98 | WFC3 F140W | 0.110 [0.139] | 0.014 [0.018] | 0.019 | 0.011 | 0.014 | 0.012 |
| 56982.32 | WFC3 F140W | 0.115 [0.147] | 0.019 [0.024] | -0.007 | 0.015 | -0.013 | 0.015 |
| 56983.18 | WFC3 F140W | 0.127 [0.161] | 0.009 [0.011] | -0.004 | 0.014 | -0.012 | 0.011 |
| 56984.84 | WFC3 F140W | 0.101 [0.128] | 0.013 [0.017] | -0.009 | 0.015 | 0.016 | 0.019 |
| 55576.98 | ACS F606W | 0.000 [0.002] | 0.026 [0.109] | 0.047 | 0.023 | -0.008 | 0.023 |
| 55619.52 | ACS F606W | -0.022 [-0.074] | 0.027 [0.113] | 0.002 | 0.020 | 0.016 | 0.028 |
| 57149.51 | ACS F606W | 0.028 [0.097] | 0.006 [0.026] | -0.013 | 0.009 | -0.001 | 0.011 |
| 57150.57 | ACS F606W | 0.042 [0.142] | 0.011 [0.046] | 0.046 | 0.008 | 0.008 | 0.007 |
| 57151.49 | ACS F606W | 0.025 [0.086] | 0.008 [0.034] | -0.019 | 0.008 | -0.002 | 0.010 |
| 57155.60 | ACS F606W | 0.035 [0.119] | 0.012 [0.048] | -0.063 | 0.009 | -0.012 | 0.010 |
| 57161.36 | ACS F606W | 0.035 [0.118] | 0.009 [0.038] | 0.047 | 0.010 | 0.004 | 0.011 |
| 57524.28 | ACS F606W | 0.108 [0.369] | 0.013 [0.053] | 0.027 | 0.016 | 0.007 | 0.015 |
| 57531.40 | ACS F606W | 0.113 [0.387] | 0.028 [0.114] | 0.062 | 0.022 | -0.001 | 0.021 |
| 57720.74 | ACS F606W | 0.014 [0.046] | 0.025 [0.103] | 0.025 | 0.021 | -0.014 | 0.031 |
| 57720.89 | ACS F606W | 0.023 [0.078] | 0.025 [0.104] | -0.035 | 0.031 | -0.008 | 0.024 |
| 53117.80 | ACS F814W | 0.038 [0.051] | 0.020 [0.031] | -0.005 | 0.021 | 0.007 | 0.019 |
| 53880.47 | ACS F814W | 0.153 [0.203] | 0.035 [0.056] | -0.036 | 0.038 | -0.026 | 0.048 |
| 57131.53 | ACS F814W | 0.074 [0.098] | 0.023 [0.036] | -0.031 | 0.020 | -0.007 | 0.021 |
| 57132.59 | ACS F814W | 0.073 [0.096] | 0.018 [0.028] | 0.004 | 0.021 | -0.001 | 0.021 |

| Date (MJD) | Bandpass | LS1/2016A Flux | LS1/2016A σ | 2016B Flux | 2016B σ | 2017A Flux | 2017A σ |
|---|---|---|---|---|---|---|---|
| 57133.79 | ACS F814W | 0.057 [0.076] | 0.024 [0.038] | 0.010 | 0.025 | 0.014 | 0.020 |
| 57134.65 | ACS F814W | 0.084 [0.112] | 0.020 [0.031] | 0.006 | 0.021 | 0.010 | 0.020 |
| 57135.58 | ACS F814W | 0.067 [0.089] | 0.026 [0.041] | -0.031 | 0.025 | -0.010 | 0.022 |
| 57137.09 | ACS F814W | 0.090 [0.120] | 0.017 [0.026] | 0.008 | 0.024 | -0.024 | 0.025 |
| 57137.63 | ACS F814W | 0.081 [0.107] | 0.025 [0.040] | -0.010 | 0.017 | 0.004 | 0.017 |
| 57137.83 | ACS F814W | 0.089 [0.118] | 0.021 [0.033] | 0.006 | 0.023 | -0.005 | 0.027 |
| 57138.09 | ACS F814W | 0.046 [0.061] | 0.020 [0.031] | 0.012 | 0.025 | -0.011 | 0.021 |
| 57140.34 | ACS F814W | 0.099 [0.132] | 0.020 [0.032] | 0.036 | 0.027 | 0.015 | 0.027 |
| 57140.61 | ACS F814W | 0.076 [0.101] | 0.021 [0.033] | 0.009 | 0.021 | 0.011 | 0.024 |
| 57141.60 | ACS F814W | 0.114 [0.152] | 0.016 [0.025] | 0.047 | 0.018 | 0.019 | 0.021 |
| 57142.46 | ACS F814W | 0.073 [0.097] | 0.020 [0.031] | -0.010 | 0.024 | -0.009 | 0.012 |
| 57143.39 | ACS F814W | 0.076 [0.101] | 0.021 [0.033] | 0.002 | 0.018 | 0.001 | 0.025 |
| 57143.66 | ACS F814W | 0.067 [0.089] | 0.012 [0.019] | -0.001 | 0.020 | 0.003 | 0.022 |
| 57149.49 | ACS F814W | 0.094 [0.124] | 0.022 [0.035] | -0.023 | 0.021 | 0.000 | 0.020 |
| 57150.55 | ACS F814W | 0.096 [0.127] | 0.026 [0.041] | -0.000 | 0.022 | 0.002 | 0.015 |
| 57151.48 | ACS F814W | 0.062 [0.082] | 0.028 [0.045] | 0.021 | 0.027 | -0.000 | 0.020 |
| 57157.39 | ACS F814W | 0.118 [0.157] | 0.022 [0.035] | -0.014 | 0.027 | -0.005 | 0.018 |
| 57159.84 | ACS F814W | 0.125 [0.166] | 0.026 [0.042] | -0.037 | 0.029 | -0.017 | 0.034 |
| 57524.34 | ACS F814W | 0.271 [0.360] | 0.037 [0.059] | -0.017 | 0.037 | 0.015 | 0.043 |
| 57524.41 | ACS F814W | 0.284 [0.377] | 0.049 [0.077] | -0.036 | 0.029 | 0.006 | 0.032 |
| 57531.49 | ACS F814W | 0.246 [0.327] | 0.043 [0.068] | 0.029 | 0.053 | -0.033 | 0.057 |
| 57720.76 | ACS F814W | 0.104 [0.139] | 0.079 [0.126] | 0.084 | 0.072 | 0.031 | 0.076 |
| 57720.87 | ACS F814W | 0.062 [0.082] | 0.071 [0.113] | 0.056 | 0.057 | 0.028 | 0.067 |
| 55605.27 | ACS F435W | 0.038 [0.267] | 0.028 [0.230] | -0.011 | 0.030 | 0.026 | 0.033 |
| 55619.53 | ACS F435W | 0.011 [0.079] | 0.034 [0.282] | -0.096 | 0.051 | -0.009 | 0.040 |
| 57131.54 | ACS F435W | 0.009 [0.061] | 0.013 [0.112] | -0.061 | 0.016 | -0.016 | 0.017 |
| 57137.11 | ACS F435W | 0.013 [0.090] | 0.015 [0.124] | -0.087 | 0.017 | -0.010 | 0.011 |
| 57138.10 | ACS F435W | 0.039 [0.271] | 0.020 [0.163] | -0.030 | 0.013 | 0.001 | 0.016 |
| 57140.36 | ACS F435W | -0.015 [-0.102] | 0.018 [0.147] | -0.014 | 0.019 | 0.022 | 0.015 |
| 57140.62 | ACS F435W | 0.011 [0.077] | 0.019 [0.156] | 0.066 | 0.016 | -0.011 | 0.014 |
| 57141.62 | ACS F435W | 0.039 [0.271] | 0.020 [0.170] | -0.109 | 0.018 | -0.007 | 0.016 |
| 57142.48 | ACS F435W | 0.011 [0.080] | 0.017 [0.142] | -0.026 | 0.018 | -0.024 | 0.018 |
| 57143.41 | ACS F435W | 0.022 [0.154] | 0.016 [0.135] | 0.196 | 0.019 | 0.033 | 0.019 |
| 57143.67 | ACS F435W | 0.029 [0.203] | 0.009 [0.073] | -0.114 | 0.016 | -0.005 | 0.015 |
| 57531.46 | ACS F435W | 0.056 [0.391] | 0.059 [0.494] | 0.215 | 0.053 | 0.010 | 0.047 |
| 56985.07 | WFC3 F606W | 0.064 [0.140] | 0.017 [0.036] | 0.005 | 0.024 | -0.005 | 0.014 |
| 56985.80 | WFC3 F606W | 0.059 [0.129] | 0.017 [0.038] | -0.001 | 0.020 | -0.019 | 0.016 |
| 57532.03 | WFC3 F606W | 0.104 [0.228] | 0.039 [0.085] | -0.009 | 0.026 | -0.015 | 0.029 |
| 57534.29 | WFC3 F606W | 0.144 [0.314] | 0.026 [0.056] | -0.001 | 0.017 | 0.014 | 0.031 |
| 57536.10 | WFC3 F606W | 0.170 [0.371] | 0.029 [0.062] | -0.013 | 0.030 | -0.007 | 0.034 |
| 57537.09 | WFC3 F606W | 0.208 [0.453] | 0.032 [0.069] | 0.038 | 0.027 | 0.011 | 0.022 |

| Date (MJD) | Bandpass | LS1/2016A | | 2016B | | 2017A | |
|---|---|---|---|---|---|---|---|
| | | Flux | $\sigma$ | Flux | $\sigma$ | Flux | $\sigma$ |
| 57580.19 | WFC3 F606W | 0.099 [0.217] | 0.023 [0.051] | -0.059 | 0.041 | 0.009 | 0.025 |
| 57592.07 | WFC3 F606W | 0.033 [0.072] | 0.034 [0.074] | 0.053 | 0.023 | 0.051 | 0.035 |
| 57756.92 | WFC3 F606W | 0.042 [0.092] | 0.035 [0.075] | 0.060 | 0.039 | 0.031 | 0.031 |
| 57776.68 | WFC3 F606W | 0.036 [0.079] | 0.030 [0.065] | -0.007 | 0.033 | -0.025 | 0.025 |
| 57853.22 | WFC3 F606W | 0.047 [0.102] | 0.035 [0.075] | 0.028 | 0.028 | 0.008 | 0.024 |
| 57872.02 | WFC3 F606W | 0.089 [0.193] | 0.035 [0.075] | -0.004 | 0.034 | -0.023 | 0.040 |
| 57892.57 | WFC3 F606W | 0.083 [0.180] | 0.033 [0.072] | -0.021 | 0.030 | 0.014 | 0.034 |

Supplementary Table 4: **Photometry at locations of LS1/Lev 2016, Lev 2016, and Lev 2017 of *HST* imaging acquired 2004–2017.** The zeropoint of listed fluxes is 25 AB, and no correction for Galactic extinction is applied. Values in brackets in LS1/Lev 2016 are estimates of star's WFC3 $F125W$ flux converted using the star's SED. For LS1/Lev16A, fluxes are the sum of flux measured from deep coaddition and that measured from a difference image created by subtracting each image from the deep coaddition. Fluxes at the positions of Lev16B and Lev 2017A are measured from difference imaging.